Mechanosynthesis of MAPbI3@Graphite Composites with Active Interfaces and Promising Photodetection Properties

Yihui Cai, Dominique Bégin, Charles Sidhoum, Adrien Girault, Thomas Fix, Christophe Lefevre, Wissal Belayachi, Aziz Dinia, Daniele Preziosi, Mathieu Gallart, et al.

Mechanosynthesis of $MAPbI_3$@Graphite composites with active interfaces and promising photodetection properties

Yihui Cai[1,2], Dominique Begin[1], Charles Sidhoum[2], Adrien Girault[2], Thomas Fix[3], Christophe Lefevre[2], Wissal Belayachi[2], Aziz Dinia[2], Daniele Preziosi[2], Mathieu Gallart[2], Pierre Gilliot[2], Eric Gros-Daillon[4], Ferdinand Ledee[4], Ovidiu Ersen[2], Clément Sanchez[5*], Sylvie Begin-Colin[2*]*

[1] Institut de Chimie et Procédés pour l'Energie, l'Environnement et la Santé (ICPEES), UMR-7515 CNRS-Université de Strasbourg, 25 rue Becquerel, 67087 Strasbourg, France.

[2] Institut de Physique et Chimie des Matériaux de Strasbourg (IPCMS), UMR-7504 CNRS-Université de Strasbourg, 23 rue du Lœss, 67034 Strasbourg Cedex 2. France.

[3] ICube, CNRS and Université de Strasbourg, 23 rue du Loess, BP 20 CR, 67037 Strasbourg Cedex 2, France

[4] CEA-Leti, Grenoble Alpes University,17 avenue de Martyrs, 38054 Grenoble, France.

[5] Sorbonne Université, CNRS UMR 7574, Collège de France, LCMCP, 4 place Jussieu & USIAS Strasbourg, France.

Abstract.

3D hybrid perovskites (HP) are currently a key player in optoelectronic applications and beyond the traditional photovoltaic applications, have also other great potentials as lighting emitting diode, lasering, photocatalyst, photo- and X-Ray-detectors. However, despite the excellent performance of 3D HP, certain HPs such as methylammonium lead iodide ($CH_3NH_3PbI_3$ named $MAPbI_3$) lack long term environmental stability because they are very sensitive to humidity and degrade under oxygen and light exposures. Moreover, $MAPbI_3$ films or monocrystal or powders are mainly elaborated from precursor mixture methods and suffer some drawbacks such as the formation of intermediate phases with solvents affecting their performance. To face some of those problems, we have optimized the synthesis of $MAPbI_3$ via a green solvent-free mechanosynthesis process, which provides also large amounts of powders, and to enhance its chemical stability, we have mixed $MAPbI_3$ with graphite, which also granted the possibility to combine the different electronic properties of both components. The mechanosynthesis parameters have been optimized for both systems to minimize the defect amount, and their structural, optical and electronic properties have been characterized. HRTEM and *in situ* HRTEM highlighted common crystallographic orientations between $MAPbI_3$ nanograins (~10 nm) in aggregates of mechanosynthesized (MS) powders. The band gap values and photoluminescence (PL) properties of mechanosynthesized $MAPbI_3$ are in good agreement with the ones reported for $MAPbI_3$ synthesized by chemical methods. A decrease in PL intensity related to the introduction of defects is observed with longer grinding time confirming that the selected grinding conditions were optimal. These mechanosynthesis conditions of $MAPbI_3$ were found also suitable to obtain $MAPbI_3$@graphite composites with different amounts of graphite. A homogeneous distribution of few-layer graphite within the $MAPbI_3$ matrix was

noticed in powder-compacted wafers. Graphite enhanced Raman scattering was observed with the composite with 5 wt% graphite showing its strong resistance to photodegradation and suggesting a charge transfer between graphite and $MAPbI_3$. Such charge transfer is also in agreement with the quenching of the PL with increasing amount of graphite.Further analysis of time-resolved PL decays confirmed, supported by X-Ray detection results, that the presence of graphite impacted the charge transfer. The presence of graphite would induce a local modification of the Coulomb interaction, "attracting" the charge carriers at the graphite and $MAPbI_3$ interfaces and thus favoring the charge separation and transport. In addition, the composite with 5 wt% of graphite exhibited promising photodetection properties with a photoresponsivity of 1.5×10^3 A/W and an effective quantum effect around 4.4×10^6 % at 400 nm with a light power of 330 nW. This high photoconductive gain matches with the trapping of one type of charge carrier, while the other one is multiplied via injection from the contact electrodes, thus contributing even more to the photoconductivity. These results highlighted that the mechanosynthesis, which is green and efficient on providing large amounts of powders, is suitable to design homogeneous $MAPbI_3$@Graphite composites with strong interactions between graphite and $MAPbI_3$ favoring an improved charge transfer and amplification of the photocurrent that will be very promising for photodetection applications.

Introduction.

In the last years, 3D hybrid perovskites (HPs) have emerged as a new class of semiconductors that show outstanding performance, giving hope of producing efficient, low-cost and flexible photonic devices. Perovskite-based organic-inorganic hybrid materials have thus become a key player in optoelectronic applications and especially for the development of efficient photovoltaic cells[1,2]. Indeed, the 3D HP family showed large absorption cross-section, long

photocarrier diffusion length, and potential high charge carrier mobility[3]. A wide range of compositions in the HP family provided a tunable band gap[4]. Thus, a real research craze on 3D hybrid perovskite materials is currently taking place but goes also beyond the traditional photovoltaic applications to extend to other applications such as LED[5–7] (light emitting diodes), photocatalysis[8–10], photodetector[11–13] or X-Ray detector[14]. Indeed, 3D HP have demonstrated very good performances as direct X-Rays detectors, exhibiting mobility-lifetime ($\mu\tau$) products, and X-Ray absorption coefficients similar to that of cadmium zinc telluride[15]. The high charge carrier mobility and the absorption properties also makes 3D HP good candidates for photodetections[11–13,16,17].

This multifunctionality makes 3D HP become an important type of materials for optoelectronic applications, but their application is limited due to the poor air-stability of lead-based HP[10,11,13,18–20]. In addition, non-stoichiometry is observed in HP film elaborated from chemical precursor mixture methods, which affect the reproducibility of HP performance. Recently, interest in HP in powder form has thus increased. As for example, they are found to exhibit high stability and allow easy production of large quantities[21,22]. However, the 3D HP powder synthesis remains a challenge due to these stability problems. Traditional HPs synthetic methods are gas-phase deposition and precipitation from solution[23]. The vapor-phase method may be difficult and complicated to realize with the use of vacuum chambers. High-quality HP crystals are needed for optoelectronic applications, but solvents used in the solution-based synthesis methods may introduce traces of water that may influence the stability of HPs. Indeed, 3D HPs degrade in the presence of water[24]. Some intermediate phases formed with solvents could also be found during the preparation of HPs, which affect their performances[25]. A thermal treatment is often needed to evaporate all the solvents and water.

Besides these methods, a new synthesis method, the mechanosynthesis[26–28], has emerged these last years for the HP synthesis. It consists in inducing the synthesis reaction by high-

energy ball milling of reactants. The main interest of mechanosynthesis (MS) is that it is a solvent free synthesis method, which can occur under inert atmosphere, and it has already been demonstrated as a promising synthesis method of HP[22–24,29,30]. As an environmentally friendly, solvent-free and energy-efficient method, MS has become a powerful alternative synthesis process of nanostructured HP powders. In addition, such synthesis method provides large amount of powder (several g/synthesis), which is a key step to envision industrial applications. During the milling process, the powders are trapped between two balls or between a ball and the vial wall. The energy generated by the collision between balls and the vial wall increases the local pressure and temperature. Highly active new surfaces are created by the rupture of particles under chocks, which, together with the transferred energy, allow inducing chemical reactions. Because of the high energy generated by the collisions and the creation of active surfaces, the MS is an efficient approach to elaborate HP with various compositions and structures. There are different types of ball-milling apparatus and different parameters may be varied during such mechanosynthesis: the materials nature of grinding tools, the rotation speed, the grinding time, the diameter and number of balls and the ball to powder weight ratio[22–24,30,31] MS is also known to introduce defects and strain in ground powders, which may affect the performance of so synthesized HPs. However, during the solar cell fabrication, mechanosynthesized HPs were shown to display an exceptional crystal quality with lower defect levels than those obtained by the solution-based method. Indeed, it is difficult to deposit exact stoichiometric perovskite thin films with this last synthesis method. It always exists a slight excess of precursor in the solution and thus, ion defects are introduced after evaporation of solvent, resulting in the formation of electron traps and enhancing non-radiative recombination. In terms of device performance, the pure-HP phase obtained by MS was reported to be promising[30].

Another problem with HP is their long-term stability. Certain HP such as $MAPbI_3$ are sensitive to humidity and thus their lifetime is much reduced [20]. In order to improve the product stability, carbon-based materials such as graphite or graphene could be a potential stabilizer because of their thermostability and hydrophobicity that could be able to prevent HPs from contact with water[32]. In addition, the combination of graphene/graphite and HP allows coupling the properties of both HP and carbon-based materials. Indeed, graphite/graphene is an attractive optoelectronic material for light detection because of its broadband light absorption and fast response time but it shows a relatively low absorption cross-section and fast recombination rate[33]. They are also excellent electron transporting materials with high electrical conductivity and thermal stability, which are frequently used in the fabrication of HP based devices but mainly under the form of an intermediate layer. Such composites are developed for solar cells[32,34–38] and also for photodetectors[11,13,33,39,40]. Most studies reported indeed on $MAPbI_3$ film or HP islands deposited on a graphene layer and only few studies have reported on $MAPbI_3$ mixed with graphene nanocrystals or graphene quantum dots[34,36,37,39–42]. All of them reported a charge transfer induced by the presence of graphene. To the best of our knowledge, homogeneous composites constituted of $MAPbI_3$ and graphite have never been synthesized by mechanosynthesis. The optoelectronic properties of such mechanosynthesized $MAPbI_3$ and $MAPbI_3$@graphite composites are interesting to compare from a fundamental point of view by tuning the graphite amount but they may also display promising properties for applications such as the X-Ray detection[43–45] that requires high thickness of wafer and for which graphite may help tuning the conductivity and as the photodetection as the formation of heterostructures between hybrid perovskite and graphene has been proved to be an effective approach to obtain performant photodetector[13,16,33,39,46].

In this work, we have established the MS conditions in a planetary ball-mill of the emblematic hybrid perovskite, $MAPbI_3$ and of the $MAPbI_3$@graphite composites by taking care of

optimizing the lowest energetic conditions to reduce the amount of defects in powders. The amount of graphite has been tuned in the composite. Their structural and optical properties under different milling conditions were characterized by standard techniques but also by high resolution transmission electron microscopy (HRTEM), X-Ray diffraction and *in situ* HRTEM as a function of temperature. The impact of graphite amount on the conductivity and optoelectronic properties have been studied by steady-state and time-resolved photoluminescence as well as Raman spectroscopy and by testing these materials as X-Ray detector and photodetector. The different characterization techniques indicated that a charge transfer occurs in the composites with graphite. The photodetection measurements evidenced further that the composite with 5 wt% graphite exhibits high gain, by comparison with MS $MAPbI_3$, with a mean photoresponsivity around 2×10^2 A/W and a mean effective quantum efficiency (EQE) value around 5×10^5 % between 1200 and 330 nm at 10V bias (even higher between 450 and 330 nm). All the results pointed to a charge carrier trapping mechanism at graphite/$MAPbI_3$ interface in this composite. MS, which is a green synthesis method, generates strong interface interactions between graphite and hybrid perovskite and allows producing several grams per synthesis, appears thus as a promising strategy to design hybrid perovskite and graphite composites exhibiting efficient charge separation and transport appealing for photodetection applications.

Experimental section

Mechanosynthesis conditions of $MAPbI_3$. $CH_3NH_3I_2$ (MAI) and PbI_2 (from TCI) (stoichiometric ratio 1:1) powders, the amount of which depends on the selected ball to powder weight ratio R, were weighted and put together in a 45 mL stainless steel milling jar with seven 15 mm diameter stainless steel balls in a glove box under an argon atmosphere. The used ball-mill is a laboratory planetary micro mill (Fritsch PULVERISETTE 7). The effect of two balls

to powder ratio have been tested: R=30 and 40. For R=30, 0.991 g of MAI and 2.873 g of PbI_2 were mixed together. For R=40, 0.743g of MAI and 2.155 g of PbI_2 were mixed together. The mixture was ground at 350 rpm for 5, 10, 15, 20, 30, 60 min and 4 h under argon. As precised above, the reactants weighting and the filling of jars were realized in a glove box under argon atmosphere and thus the MS was realized under argon atmosphere. The resulting powders were stored in a glove box under argon atmosphere.

Mechanosynthesis of $MAPbI_3$@Graphite composites. Graphite (Timcal (Imerys group)) powder, MAI and PbI_2 (stoichiometric ratio MAI: PbI_2 = 1:1) powders were introduced in the vial under argon atmosphere. The mixture was ground for 30 min at 350 rpm with a ball to powder weight ratio of 40. The amount of graphite has been varied in the reactant mixture. 13.31 mg of graphite, 0.679 g of MAI and 1.969 g of PbI_2 were mixed together for the preparation of $MAPbI_3$@Graphite 0.5%. 20.07 mg of graphite, 0.677 g of MAI and 1.964 g of PbI_2 were mixed together for the preparation of $MAPbI_3$@graphite 0.75%. 26.62 mg of graphite, 0.676 g of MAI and 1.959 g of PbI_2 were mixed together for the preparation of $MAPbI_3$@graphite 1%. 0.133 g of graphite, 0.648 g of MAI and 1.880 g of PbI_2 were mixed together for the preparation of $MAPbI_3$@graphite 5%. All syntheses were realized under argon atmosphere and the resulting powders were stored in a glove box under argon atmosphere.

X-Ray diffraction (XRD). XRD patterns were collected using BRUKER D8 DISCOVER equipped with a copper X-Ray anode ($K_{\alpha 1}$ = 0,154056 nm), a motorized anti-scatter screen and Johansson monochromator. The measurements employed a θ-θ Bragg–Brentano geometry, and a Lynxeye XE-T energy-resolved linear detector to filter the fluorescence. Diffraction patterns were measured in the 5 to 90 degrees in 2θ with a step of 0.02 degree. The nature of crystalline phases can be identified by XRD. Lattice parameters, mean crystallite size and strain were obtained from experimental data using the Fullprof software. Le Bail analysis has been

performed and a Thomson-Cox-Hasting (TCH) function has been chosen for the profile. An internal standard instrumental contribution was measured by corundum.

UV-visible diffuse reflectance spectroscopy and band gap determination. Ultraviolet-visible diffuse reflectance spectroscopy was performed using a Perkin Elmer Lambda 950 UV/Vis Spectrometer using the STD Detector Assy. The spectral range was from 300 nm to 1000 nm. The measured reflectance spectra were transformed into corresponding absorption spectra by applying the Kubelka–Munk function: $F(R_\infty) = \frac{K}{S} = \frac{(1-R_\infty)^2}{2R_\infty}$ where K stands for the absorption coefficient and S is a semi-empiric scattering coefficient. R_∞ is the reflectance of an infinitely thick specimen: $R_\infty = \frac{R_{sample}}{R_{standard}}$. The band gap energy determination is based on the Tauc method where energy-dependent absorption coefficient α can be expressed by: $(\alpha \cdot h\nu)^{1/\gamma} = B(h\nu - E_g)$, where h is the Planck constant, ν is the photon's frequency, E_g is the band gap energy, and B is a constant. The γ factor equals to ½ because $MAPbI_3$ is a direct-band semiconductor. By replacing α with $F(R_\infty)$ and plotting $(F(R_\infty) \cdot h\nu)^{1/\gamma}$ as a function of E_g, the x-axis inter- section point of the linear fit of the Tauc plot gives an estimated band gap energy.

Raman spectroscopy. The Raman spectra were obtained using a LabRAM ARAMIS Horiba Jobin Yvon Raman spectroscopy with a 532 nm wavelength excitation source. A 4 mW laser power was used to study Raman graphite bands and $MAPbI_3$ bands in the composite of 5 wt% graphite. The laser power for $MAPbI_3$ bands characterization was reduced to 0.04 mW for $MAPbI_3$ alone and the composite with 1 wt% graphite as a photodegradation under stronger laser power was observed.

Wafer preparation. The ground powders were uniaxially compressed into wafers of 7 mm diameter for photoluminescence, time-resolved PL transport and SEM measurements and X-Ray detection performance. 0.1g of each powder specimen were precisely weighted and

compressed under a pressure around 100MPa by using an uniaxial press with a 7mm diameter cylindrical mould.

Photoluminescence (PL) measurement. The measurements on mechanosynthesized $MAPbI_3$ wafers were performed with a 355 nm wavelength excitation source and a laser power of 65 mW. For the $MAPbI_3$@graphite composite wafers, the measurement conditions were: a 320 nm wavelength excitation source and a laser power of 130 μW. All the PL measurements were performed on compacted wafers.

Time-resolved PL spectra. The time resolved photoluminescence spectra of compacted wafers were obtained using a spectrometer paired with a Hamamatsu streak camera (C10627) synchronised with the excitation pulse. The 270 femtosecond UV (320nm) pulse is generated by mixing the second harmonic of a 1030nm pulsed Ytterbium laser with a continuum. The repetition rate has been set to 10 kHz and a photon counting mode was used to make the acquisition.

Transport measurements. Temperature-dependent resistance measurements have been performed by using a cryogen-free DynaCool System from Quantum Design. A Van der Pauw geometry was used for the silver top-electrodes deposited on both $MAPbI_3$ wafer and related composites. A very small current of 0.5 μA was applied to the outermost electrodes to account for the relatively large resistance value of the measured systems.

Transmission electron microscopy (TEM). The HP and composite powders were characterized by transmission electron microscopy (TEM) using a LaB_6 microscope operated at 200 kV. The samples were deposited on a holey carbon-coated TEM grid. In addition to the classical TEM images, selected area electron diffraction (SAED) patterns were also obtained by selecting the areas of interest; dark-field TEM images were finally acquired by considering a specific diffraction spot.

In situ high resolution TEM (HRTEM) images and SAED patterns were acquired on a corrected JEOLF/Cs TEM operating at 200kV. The TEM grids were placed on a Gatan single-tilt heating holder. The temperature is reached by resistive heating and monitored by thermocouple measurement with a precision of 1°C.

Scanning electron microscopy (SEM). Scanning Electronic Microscopy (SEM) was used to observe as-mechanosynthesized powders and compacted powders using a Zeiss Gemini SEM 500 scanning electronic microscope and a JEOL 6700F scanning electronic microscope both operating at 3.00 kV. The COMPO mode was performed with the diode detector collecting only the backscattered electrons, thus revealing the chemical contrast. The compacted wafers were manually broken to observe cross-sections.

X-Ray Detection performance. Cr/Perovskite/Cr devices were fabricated by thermally evaporating chromium (100 nm) on both sides of a compacted wafer through a physical mask. The devices were mounted inside a faraday box for the X-Ray induced photocurrent measurement. The X-Rays were generated with a medical-grade pulsed X-Ray tube with a tungsten anode, operated at 70 kV and with additional 23.5 mm Al filters (RQA5 spectrum). Each acquisition consisted on irradiation with 10 subsequent pulses of X-Rays at 4 Hz repetition rate and 100 ms pulse duration (24 μGy per pulse). The tube output dose was calibrated with a PTW Unidos ionization chamber. The current flowing in the devices was measured with a Keithley 428 current amplifier and Keithley 487 power supply. The photocurrent resulting from the irradiation was averaged over 10 pulses to reduce experimental noise.

Photodetection performance. The I–V characteristics of the samples were obtained using an AAA rated ORIEL Verasol-2 LED Solar Simulator (LSS-7120) in AM1.5G conditions and a Keithley 2461 Source Measure Unit.

Photoresponsivity was recorded on a External Quantum Efficiency (EQE) setup including a light source (tungsten halogen) and automated filter wheels with sorting filters in an appropriate

order; 41 filters are employed for the measurements and the current is measured with a Keithley 2450 SourceMeter. Photoresponsivity is calculated as follows $(I-I_{dark})/P$ where I and I_{dark} are the current under illumination and in dark and P is the light power at a given wavelength estimated from the EQE of a certified reference detector at the same wavelength.

Results and discussions

1 Mechanosynthesis and characterization of so obtained $MAPbI_3$.

Influence of milling time and ball to powder weight ratio R. The evolution of crystalline phases in the reaction media has been followed by XRD as a function of grinding time and the balls to powder ratio R. The XRD pattern of the powder ground for 10 min with R= 30 is given in Figure S1A and the XRD peaks are indexed with PbI_2, MAI and $MAPbI_3$ phases. No other phases are identified showing that the formation of tetragonal $MAPbI_3$ would occur without intermediate phases by contrast to what was observed during the chemical syntheses in solution[25]. With increased grinding time, the intensity of the XRD peaks of PbI_2 decreases when that of $MAPbI_3$ increases as can be observed in Figure S1B. After grinding for 30 min with R=30, only the XRD peaks of a well-defined $MAPbI_3$ are identified. Only this phase was also observed after grinding with R=40 for 30 min, 60 min and 4h. With R=40, the chemical reaction was almost finished after grinding for 15 min while for R=30, after grinding for 20 min some reactants are still identified in the milled powder. This is in agreement with the more energetic conditions provided by R= 40 in comparison with R=30. A grinding time of 30 min appears optimal for both R ratios. Longer grinding times have been performed for R=40 to study the effect of grinding time on the nanograin size and defects in MS powders.

The lattice parameters have been determined from XRD patterns fitting as well as the mean crystallite size and strain (Table 1). The lattice parameters of mechanosynthesized HPs are close to those in the JCPDS card n°01-085-5507. The lattice strain increases when R increases and

seems to saturate after grinding for 30 min (Table 1), but in all cases, the strain values are very low. Such weak lattice strain values could be explained by the hybrid nature of HP with the presence of the organic part providing flexibility and damping capacities. The mean crystallite sizes are observed to increase with R and tend to stabilize with grinding time for R=40. However, a decrease in crystallite size with the grinding time was often observed during the simple grinding of metallic oxide powders due to the fracture and welding events[47]. Such a "stabilization" of crystallite size should be due to the hybrid nature of $MAPbI_3$, which makes the fracture and welding process not similar and less efficient. Indeed, the strong chemical interactions between the ammonium and the lead iodide components should make the welding between reactive surfaces effective and thus an equilibrium between fracturing and welding occurs with grinding time. Another hypothesis would be that, as soon as the HP phase is formed, the fracture and welding mechanisms do not occur anymore and the powders are just submitted to chocks during the grinding process.

Table 1. Lattice parameter, mean crystallite size, strain and band gap (UV spectra) of $MAPbI_3$ as a function of grinding conditions.

	Lattice parameter (Å)	Crystallite size (nm)	Strain (%%)	Band gap (eV)
$MAPbI_3$ JCPDS card N°.01-085-5507	a=b=8.8660, c=12.6524	--	---	1.50-1.60
R=30, t= 30 min	a=b=8.878±0.001, c=12.675±0.001	90 ±1	3.4±0.1	1.53
R=40, t= 30 min	a=b=8.873±0.001, c=12.670±0.001	136±1	10.0±0.1	1.55
R=40, t= 60 min	a=b=8.874±0.001, c=12.664±0.001	137±1	16.6±0.1	1.54

R=40, t= 4 h	a=b=8.875±0.001, c=12.662±0.001	147 ±2	16.4±0.1	1.54

Optical properties. In Table 1, are given the band gaps deduced from the Tauc's plots of $MAPbI_3$ prepared under different milling conditions. These values are in good agreement with those reported for $MAPbI_3$ in the range 1.5-1.6 eV[48]. Prochowicz *et al.*[30] also synthesized $MAPbI_3$ through ball milling, and reported a band gap of 1.48 eV. They explained this lower value by the presence of defects. Jodlowski *et al.*[23] obtained a $MAPbI_3$ powder with a band gap of 1.51 eV by using a similar planetary ball mill. The obtained values for our $MAPbI_3$ powders could suggest a low defect density.

The PL spectra of the $MAPbI_3$ powders ground for 30 min with different ratios R= 30 and 40 and compacted under the form of wafers showed a strong exciton emission at 1.585 eV and 1.636 eV respectively (Figure 1A). These values are in the range of PL peak position reported for different synthesis methods between 700 to 800 nm (1.55 - 1.77 eV)[49–54]. The slightly higher values obtained by PL measurements in comparison with those deduced from UV-Vis spectra is explained by the compaction of powders in wafer for performing steady-state and time-resolved photoluminescence experiments. Indeed, the PL and UV-Vis spectra in Figure S2, performed on powders, show the expected curve positions and confirmed that the compaction is responsible for the small shift of the PL peak. Such a blueshift of the PL emission peak induced by compaction was suggested to be due to a structural distortion in the tetragonal phase of $MAPbI_3$ under high-pressure conditions.[55] The change of particle size and thickness during the wafer-making process was also reported to influence the PL emission properties[56–58].

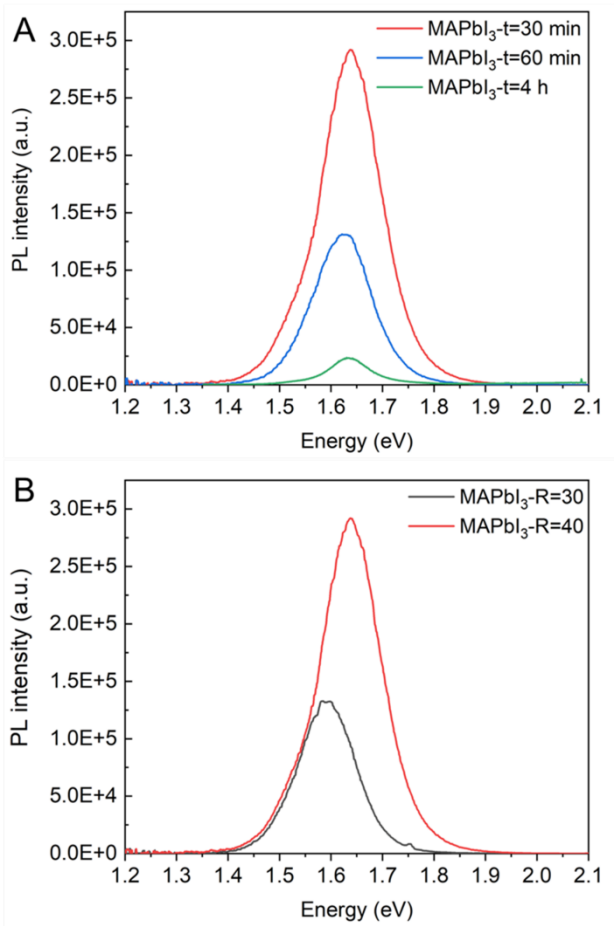

Figure 1. PL spectra of $MAPbI_3$ as a function of A) R (black: R=30, red: R=40) after grinding for 30 min and B) milling time (red: t=30 min, blue: t=60 min, green: t=4 h) with R=40.

The maximum PL peak shifted with R values after 30 min of grinding as was also slightly observed with the band gap values. The spectrum of $MAPbI_3$ milled for 30 min also displays a less intense peak with R= 30 than with R=40. That may be explained by the fact that the reaction might not be thoroughly finished after grinding for 30 min with R=30 when it is the case with R=40. The remaining precursors amount was certainly under the detection limit of XRD or the products were not crystallized enough. The PL spectra of $MAPbI_3$ milled with R= 40 and for t=30 min, 60 min and 4h present PL peaks at quite the same maximum value positions (1.636, 1.621, 1.635 eV respectively) and the PL peak intensity decreases when the milling time increases (Figure 1B). Such a decrease in PL intensity could reveal a phenomenon of non-

radiative recombination, and the presence of defects is often reported to be responsible for such charge recombination[59–61]. To further confirm the presence of defects, the Urbach energy has been calculated from UV-Vis spectra and is observed to increase with grinding time from 23.1 to 36.3 meV after grinding for 30 min and 4h respectively. The values reported for $MAPbI_3$ in thin films are in the range of 13-17 meV[62–65], values of 22.4 meV and ~33 meV were noticed with wet milled and in mortar ground $MAPbI_3$ respectively[66,67]. The Urbach energy of $MAPbI_3$ mechanosynthesized for 30 min (23.1 meV) is lower than that reported for solvent-free ground powders (~33 meV)[67], confirming the lower level of defects of this MS powder obtained by optimizing the synthesis conditions in comparison with that ground for 4h. These results confirmed that, even if the bandgap values are in the proper range of reported experimental values, PL measurements showed that long milling times would induce the presence of defects in MS. Enhanced reabsorption phenomena are also not to exclude[60,68]. Indeed, the milling process generates local high pressure and leads to the formation of aggregates. The grain boundaries in aggregates formed during the grinding process may also contribute to the non-radiative recombination of charge carriers and reabsorption phenomena. According to these PL spectra, the $MAPbI_3$ powders mechanosynthesized at R=40 and t=30 min showed the highest PL performance with the appropriate bandgap value and good crystallinity. Therefore, an optimal synthesis condition was determined based on the adjusted parameters, which provided enough mechanical energy to induce the chemical reaction without introducing too many defects.

Powder morphology. SEM image of ground powders (Figures S3A&B) confirmed the presence of large particles constituted of micrometric aggregates with a mean particle size of 340 ± 50 nm. The air stability of these mechanosynthesized $MAPbI_3$ powders was followed by XRD analysis and they were found stable for more than 2 weeks, which can be explained by the aggregation state of ground powders. Figure S3C presents the dense microstructure of a

cross-section of a wafer (obtained by uniaxial compaction of MS powders) used to perform PL and X-Ray detection measurements. Indeed, the MS powders exhibited excellent compressibility leading to quite dense wafers, (calculated density of ~4 g/cm^{-3} similar to that of single-crystallin $MAPbI_3$: 4.15 g/cm^{-3} calculated form lattice parameters[43]), which could notably ease the fabrication of devices based on HP wafers.

The formation of aggregates was also confirmed by TEM in the bright and dark-field modes. Some typical images, shown in Figures 2A-C, underlined that the MS powders consist of micron-scale aggregates of nanocrystals with a mean size of ~ 5 nm. Moreover, the analysis by high-resolution TEM (Figures 2D-H) demonstrated that the nanocrystals in mechanosynthesized $MAPbI_3$ aggregates display an oriented aggregation. Indeed, common crystallographic orientations between nanograins are observed in Figures 2E-G (see arrows), confirmed by the SAED pattern in Figure 2D and by the mosaicity with a mean angular deviation of ~20° noticed from the fast Fourier transform (FFT) analysis on HRTEM images (Figure 2H). Such oriented aggregation is also supported by the fact that the mean TEM nanograin size is of about 5 nm when the mean crystallite size determined from XRD pattern (Table 1) is higher. Such discrepancy may be explained by an oriented aggregation of nanograins as already observed in iron oxide nanoclusters[69,70].

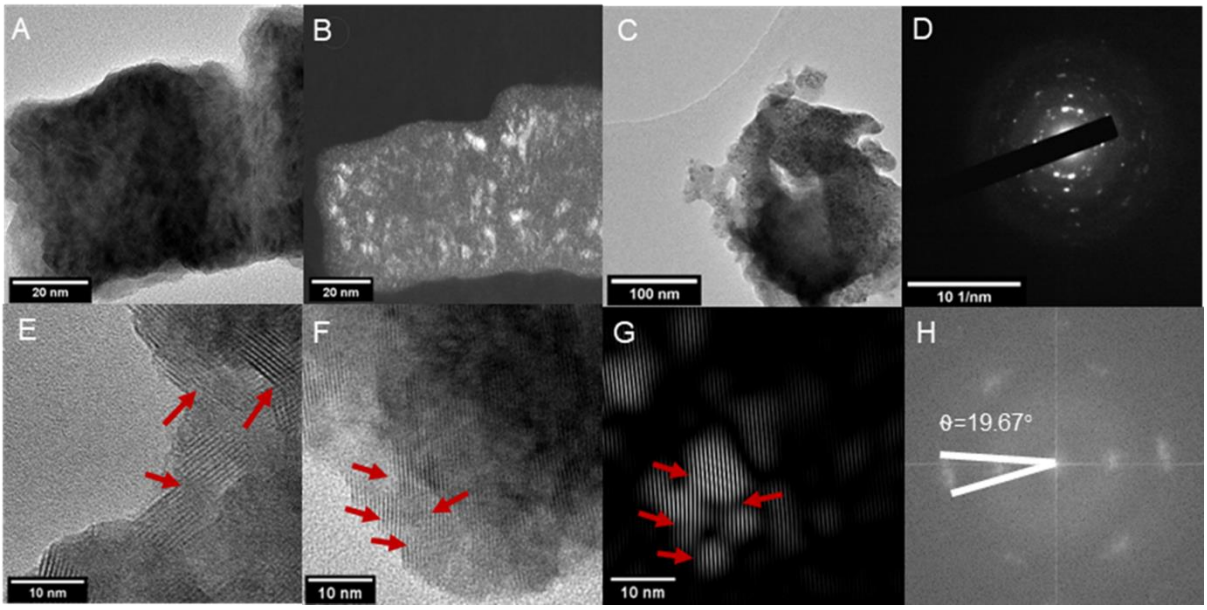

Figure 2. A) Bright-field and B) dark-field TEM images, C) TEM image and D) the corresponding SAED pattern, E) HRTEM image of some aggregates in powders ground at R=40 and t= 30min, F) HRTEM image of an aggregate with G) the corresponding filtered high-resolution images obtained from FFT analysis and H) the corresponding FFT images.

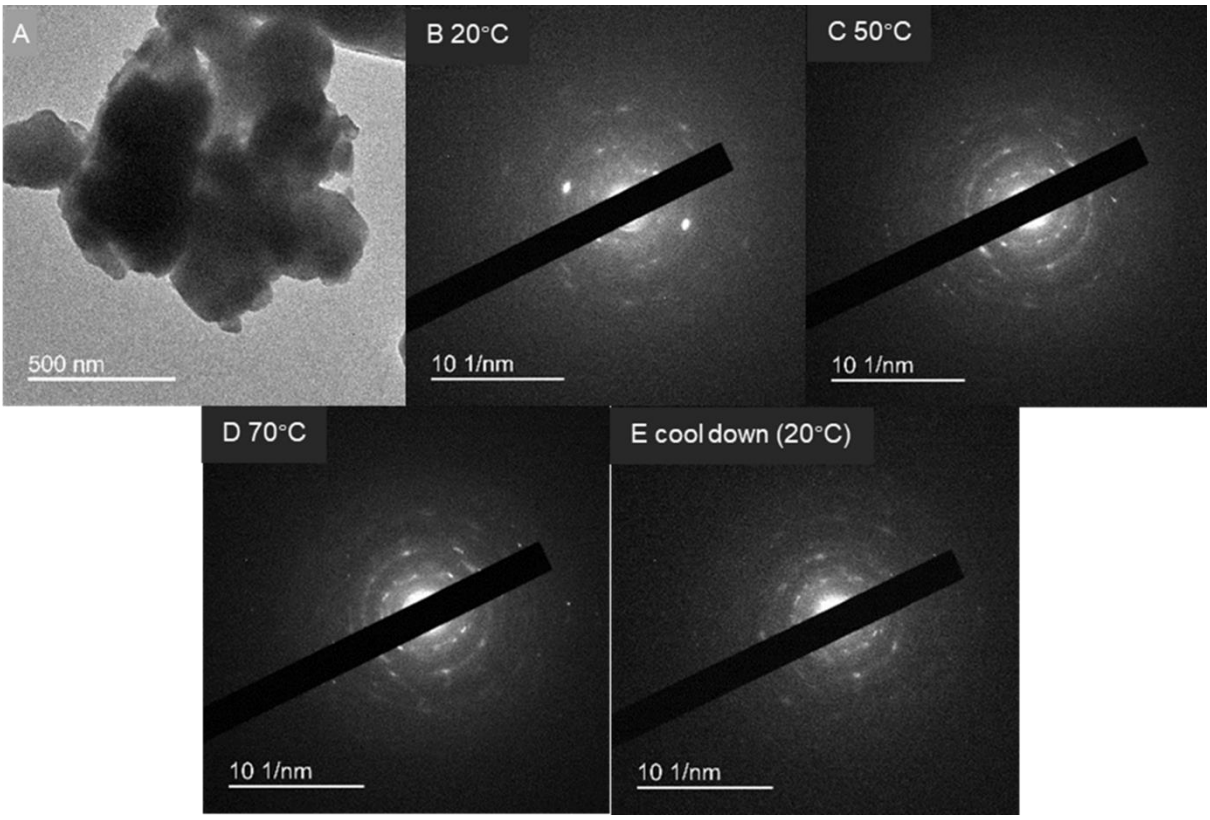

Figure 3. A) TEM image and the corresponding SAED patterns at B)20°C, C) 50°C, D) 70°C and E) cool down at 20°C of a $MAPbI_3$@Graphite 1 wt% aggregate from powders ground with R=40 and t= 30min.

To further investigate the crystallographic orientations in the aggregates and observed a possible coalescence within aggregates favored by this oriented aggregation of nanograins, an *in situ* heating analysis was carried out by TEM by monitoring a typical aggregate of the composite powder of $MAPbI_3$@graphite with a doping concentration of 1wt % in graphite. The addition of graphite provided a higher stability of $MAPbI_3$ under the electron beam as the graphite processes excellent electrical conductivity. Thus, it helped to evacuate the electrical charges, which accumulate in hybrid perovskites and represent a well-known cause of the $MAPbI_3$ degradation under the electron beam[71]. The selected area electron diffraction (SAED) patterns performed on the same aggregate heated at different temperatures are given in Figure 3 and revealed the irreversible loss, under heating at low temperature, of the oriented aggregation of nanograins in aggregates. Indeed, the SAED patterns (Figures 2D and 3B) with typical characteristics of an almost monocrystalline structure (intense diffraction points and no clear diffraction rings) evolved towards those of a polycrystalline structure displaying well defined diffraction rings. This was further confirmed by visualizing the filtered HRTEM images, obtained via a FFT analysis, of the same aggregate at different temperature by selecting some specific spots (Figure 4). The as obtained images before heating at 20°C confirmed the oriented aggregation of nanograins and, during the heating treatment, a coalescence between the grains sharing common crystalline plan orientation is observed in agreement with SAED patterns analysis.

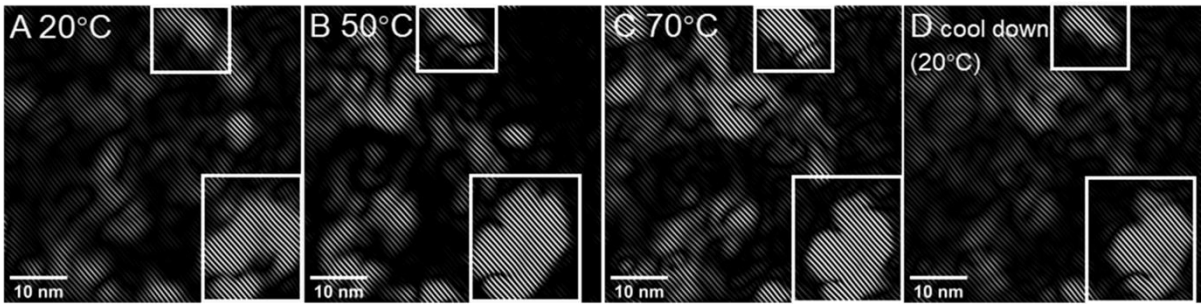

Figure 4. Filtered high resolution images, obtained from a FFT analysis, corresponding to A) 20°C, B) 50°C, C) 70°C and D) cool down at 20°C of $MAPbI_3$@Graphite 1 wt% powder for R=40 and t= 30min.

The thermal behaviour of MS powders has also been studied by X-Ray diffraction. XRD patterns as a function of temperature in Figure S4 indicated that the ground $MAPbI_3$ powder exhibited a reversible phase transition: the $MAPbI_3$ passed through the room-temperature tetragonal structure to a cubic structure at temperatures higher than 55°C. It is demonstrated by the change of the double XRD peaks at 28.1° and 28.4 ° and at 31.6° and 31.8°, merging both into a single peak at 28.3° and 31.8° respectively, when the temperature is higher than 55°C in agreement with published results[72]. The refiniment of XRD patterns showed a slight increase of the cristallite size in the ground powder under heating (Table 2) suggesting again the coalesence between nanograins leading to the transition to the polycrystalline structure observed in TEM.

Table 2. Mechanosynthesized $MAPbI_3$ mean crystallite size variation with temperature.

	25°C	50°C	70°c	25°C (cool down)
Crystallite size (nm)	158±1	222±1	180±1	178±1

2 Mechanosynthesis of $MAPbI_3$@Graphite composites

Influence of graphite amount. The grinding experiments with different amounts of graphite have been conducted with R=40 and a grinding time of 30 min as previously established for $MAPbI_3$ mechanosynthesis. After milling for 30 min, no XRD peaks of reactants are observed in all XRD patterns (Figure S5), which display, whatever the amount of graphite, the characteristic XRD peaks of the tetragonal structure of $MAPbI_3$ confirming the formation of the HP phase by ball-milling. Therefore, the $MAPbI_3$ reaction kinetics appears not affected by the presence of graphite in the reaction medium. The XRD peaks of graphite were not observed in all the XRD patterns as the graphite concentration stays below the XRD detection limit of 5 wt%. The lattice parameter, crystallite size and strain of $MAPbI_3$ obtained from the refinement of XRD patterns are given in Table 3. The lattice parameters are similar whatever the amount of graphite and correspond to those of mechanosynthesized $MAPbI_3$. The lattice strain remains low and is even lower than that of MS $MAPbI_3$. The crystallite size is in the range 100-150 nm as with MS $MAPbI_3$.

Table 3. Lattice parameter, crystallite size and strain of $MAPbI_3$ from analyses of XRD patterns in different composite samples (grinding conditions: R=40 and t=30 min).

	5 wt% graphite	1 wt% graphite	0.75 wt% graphite	0.5 wt% graphite	MS $MAPbI_3$
Lattice parameter (Å)	a=b=8.871±0.001, c=12.669±0.001	a=b=8.872±0.001, c=12.667±0.001	a=b=8.872±0.001, c=12.666±0.001	a=b=8.872±0.001, c=12.666±0.001	a=b=8.873±0.001, c=12.670±0.001
Crystallite size (nm)	132 ±1	126 ±2	153 ±3	151±3	136 ±1
Strain (%%)	5.6±0.1	7.8±0.1	6.8±0.1	8.2±0.1	10.6±0.1

Composites microstructures. TEM images, as illustrated in Figures 5 and S6, showed the presence of the light grey graphite sheets demonstrating that the milling conditions with the composite reactants has succeeded in partially exfoliating the bulk graphite. The milled graphite sheets displayed only very few layers. The dark phase in Figure 5 corresponds to the $MAPbI_3$ one and TEM images evidenced a quite good mixing/interaction of both graphite sheets and $MAPbI_3$.

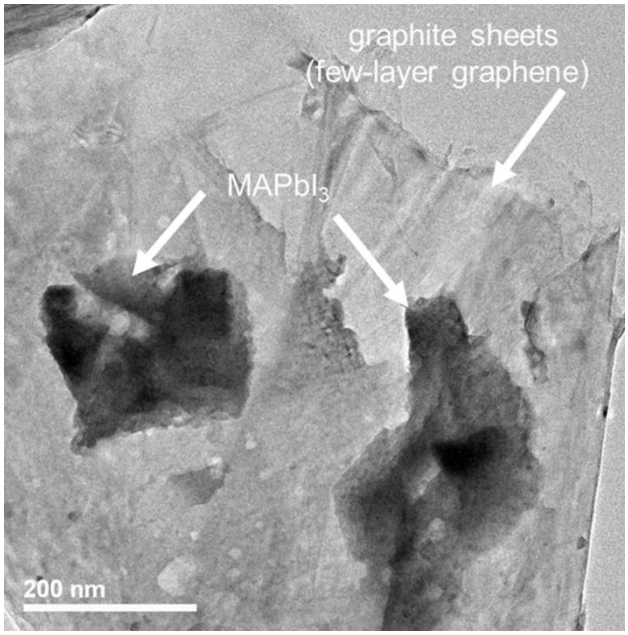

Figure 5. TEM image of the mechanosynthesized composite with 1 wt% of graphite.

The comparison of SEM images in COMPO mode and at high magnification (Figure S7) of MS $MAPbI_3$ and $MAPbI_3$@graphite composites showed that the presence of graphite induced the formation of aggregates with a smaller mean size: ~268 nm, ~220 nm, ~219 nm and ~133 nm ±70 nm for graphite content of 0.5 wt%, 0.75 wt%, 1 wt% and 5 wt% respectively (the mean size was ~340 nm for MS $MAPbI_3$). This suggested that the presence of graphite reduced the aggregation of powders. SEM images in COMPO mode and at lower magnification (Figure 6) of the surface of wafers revealed a quite homogeneous distribution of graphite sheets along the wafer section in all the samples whatever the graphite concentrations. These observations

demonstrated that the milling process under the optimal condition was very efficient to prepare homogeneous $MAPbI_3$@graphite composites (Figures S7 and 6).

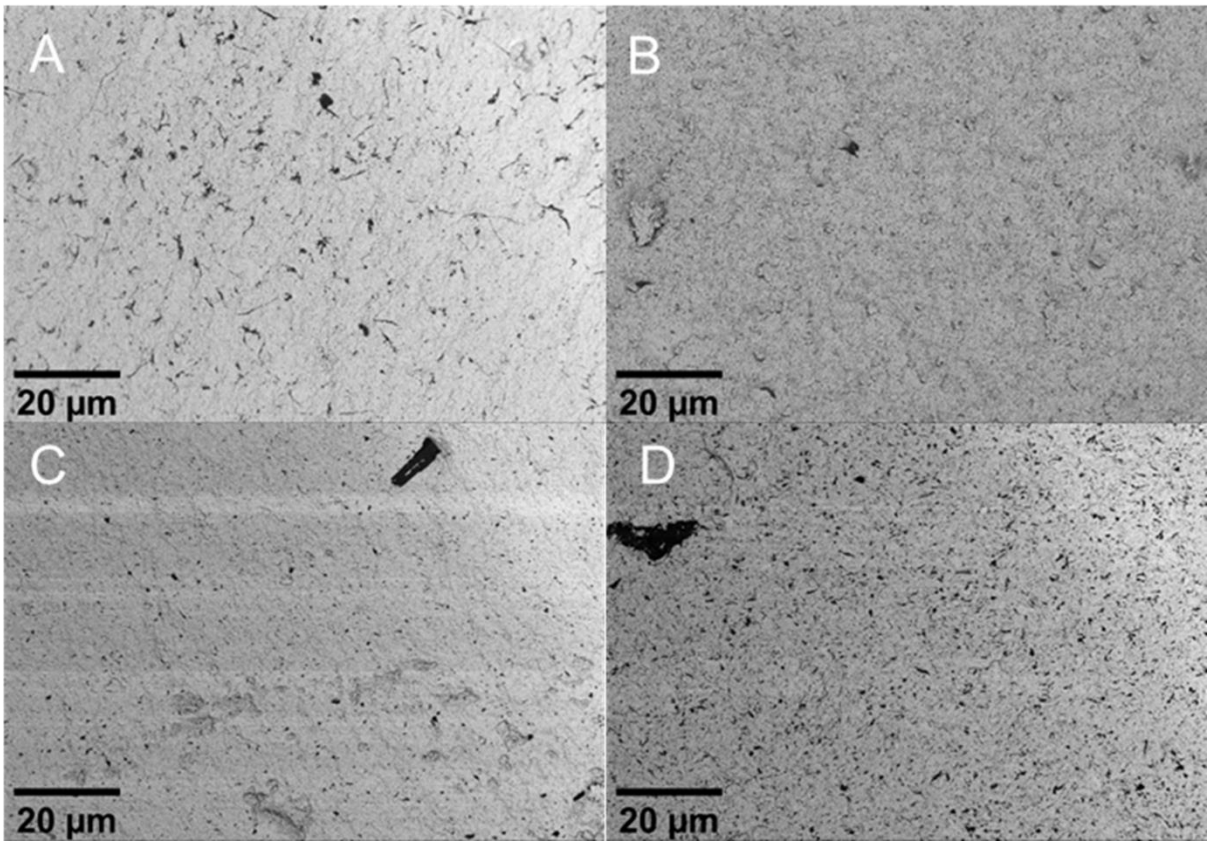

Figure 6. SEM images in COMPO mode of $MAPbI_3$@Graphite wafers of A) 0.5 wt% graphite, B) 0.75 wt% graphite, C) 1 wt% graphite and D) 5 wt% graphite ($MAPbI_3$ correspond to the white phase and graphite to the black phase).

Raman spectroscopy was then used to check the effect of milling on $MAPbI_3$ and on the composites. For comparison, a milling of only graphite in the same conditions was also carried out. The Raman spectra of ground graphite displayed two bands at 1350 and 1580 cm^{-1} named D (for Defects) and G (for Graphite) bands respectively (Figure S8). The D band around 1350 cm^{-1} gives indication about the presence of defects in graphite. In order to evaluate the defect level, the D/G band intensity ratio (I_D/I_G) of each sample has been calculated and is reported in Table 4. The unground graphite displayed quite no defects and, after grinding for 30 min, quite no defects are detected (I_D/I_G = 0.08 and 0.09 for unground and ground graphite respectively).

However, as soon as a very small amount of graphite (0.5%) is introduced during $MAPbI_3$ mechanosynthesis, this ratio strongly increases with the amount of graphite and seems to saturate. It is quite surprising because the grinding of graphite alone did not induce such variation. To better analyze Raman results, the G and 2D bands have been carefully analyzed in Figure 7. 2D band, which is located at about 2700 cm^{-1}, comes from a second order process involving two phonons. A shoulder is observed in the G band around 1610 cm^{-1} which is generally attributed to the D' band. According to Eckmann *et al*[73]., the amplitude intensity ratio of D band and D' band, $I_D/I_{D'}$, gives information on the defect type in the graphene layers. The $I_D/I_{D'}$ values of composites with 0.75, 1 and 5 wt% of graphite is around 3.5 (Table 4), suggesting that the defects in the few-layer graphene could origin from grain boundaries between the graphite grains[73].

The band position (Table 4) could also provide information on the few-layer graphene properties: when there are intercalant species interacting with graphene, the charge density change introduced by the reactive species could cause the upshift of G and D' bands, while the strain induced by the intercalant process could result in the downshift of the band. For the 2D band, only the downshift could be observed as the charge has a minor influence on the 2D band[74]. By comparing these three band positions among graphite, milled graphite and the $MAPbI_3$@graphite composites, no obvious shift has been observed in the G band position while all the D' bands of the composite have upshifted of around 10 cm^{-1} suggesting a charge density change. Downshifts of around 10 cm^{-1} of 2D band are also noticed in all the composites, which indicates that strains have been introduced into the graphite lattice. These both observations could be the hint of the successful insertion of $MAPbI_3$ in between the graphite layers and suggested a strong interaction between $MAPbI_3$ and graphite as also suggested by TEM images.

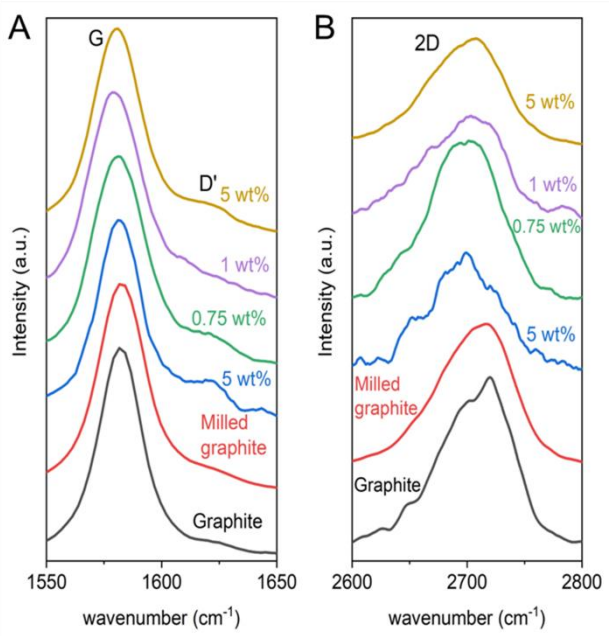

Figure 7. Raman spectra: A) G and D' bands and B) 2D band of graphite, milled graphite and $MAPbI_3$@Graphite composites with different graphite amounts.

Table 4. D/G band intensity ratio I_D/I_G, D/D' band intensity ratio $I_D/I_{D'}$, G band, D' band and 2D band maximum positions of graphite in the different samples (grinding conditions: R=40 and t=30 min).

	Graphite	Milled graphite	5 wt% graphite	1 wt% graphite	0.75 wt% graphite	0.5 wt% graphite
I_D/I_G	0.08	0.09	0.42	0.42	0.32	0.31
$I_D/I_{D'}$	0.74	0.73	4.91	3.10	3.59	1.72
G band (cm^{-1})	1581.8	1578.6	1580.6	1579.5	1581.2	1581.6
D' band (cm^{-1})	1613.9	1603.9	1619.1	1611.0	1617.8	1618.7
2D band (cm^{-1})	2708.9	2706.2	2698.7	2697.7	2697.7	2697.4

Raman spectroscopy was also carried out in the range 0-500 cm^{-1} for ground $MAPbI_3$ and two composites doped with 1% and 5% graphite (Figure 8). The spectrum of $MAPbI_3$ alone displayed a low resolution as often reported, which would be due to the strong absorption of HP leading to decomposition or phase transformation and to the strong photoluminescence nature of hybrid perovskite[75–78]. Indeed, the photodegradation tendency of $MAPbI_3$ makes it difficult to obtain well-resolved Raman spectra, even if calculated Raman spectra reported well-resolved spectral features[76,79]. The very broad and weak band at ~100 cm^{-1} could be attributed to the Pb−I stretching modes and the very broad and weak one at around 250 cm^{-1} to the torsion mode of the methylammonium cation[75]. Surprisingly, intense and better-resolved bands are observed in the Raman spectra of composites. For the sample with 1 wt% graphite, the two bands at 95 cm^{-1} and 110 cm^{-1} and the weak band at 166 cm^{-1} are characteristic of PbI_2, the main degradation product of $MAPbI_3$ [76–78]. The spectrum of the composite with 5 wt% graphite is very different from the previous one with no characteristic peaks of PbI_2 and it matchs quite well with Raman spectra reported for $MAPbI_3$ [76,79]. Four bands are identified: the one at 81 cm^{-1} is attributed to the asymmetric stretching mode of Pb-I and that at 135 cm^{-1} to the libration mode of methylammonium[75,78,79]; the two weak and broad bands at 266 cm^{-1} and 363 cm^{-1} might be associated to torsional modes of methylammonium as they are predicted to be present in the range 200-400 cm^{-1} [79].

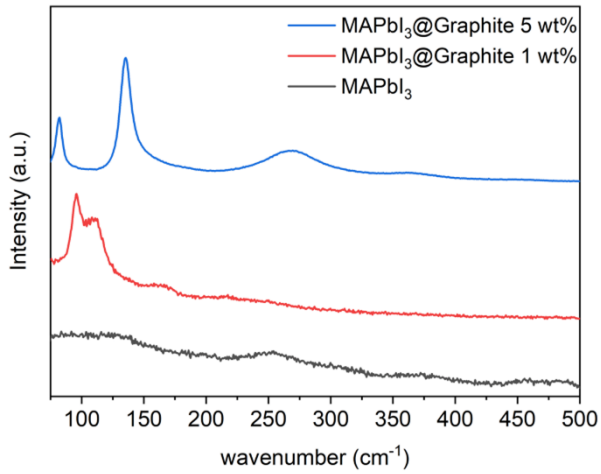

Figure 8. Raman spectra of $MAPbI_3$ and $MAPbI_3$@Graphite composites with two different graphite amounts.

The observed photodegradation of the composite with 1 wt% of graphite when no degradation is noticed with the composites with 5 wt% of graphite suggested that 5% graphite allowed limiting the degradation of $MAPbI_3$ even under higher laser power (4 mW compared with 0.04 mW for bare $MAPbI_3$ and the composite with 1 wt% graphite). The better-resolved Raman spectra with composites by comparison with the one of $MAPbI_3$ alone evidenced an enhancement of the Raman spectra induced by the presence of graphite (graphene-enhanced Raman scattering) and thus would point to strong interactions between graphite and $MAPbI_3$. Indeed, it has already been reported that graphene could enhance the Raman spectroscopy and that charge transfer could occur during the Raman scattering[80]. Similar results have also been reported by Kim *et al.*[81] with the $CsPbI_3$ perovskite and such chemically induced signal enhancement would be possible via rapid charge transfer through the molecule/graphene interface. It has also been noticed that graphene could help suppressing the self-absorption of certain organic dyes under the Raman scattering conditions[82], which might explain why high quality Raman spectra have been obtained in the composite as the strong absorption of $MAPbI_3$ is one of the main issues of Raman scattering.

Optical and electronic properties. The bandgap values extracted from the Tauc's plots of $MAPbI_3$@graphite prepared with different graphite amounts (Table 5) are similar to the one of $MAPbI_3$ synthesized alone with the same synthesis parameters and are in agreement with reported experimental values[50,52,83].

In PL spectra obtained on compacted MS powders in wafers (Figure 9A), the PL peak at 1.623 eV, 1.627 eV 1.637 eV and 1.641 eV for $MAPbI_3$@graphite 0.5 wt%, $MAPbI_3$@graphite 0.75 wt%, $MAPbI_3$@graphite 1 wt% and $MAPbI_3$@graphite 5 wt% are in good agreement with

expected $MAPbI_3$ emission value, indicating again the formation of $MAPbI_3$ even in presence of graphite. As mentioned before, the upshift of PL peaks is due to the wafer compressing process. However, a PL quenching phenomenon is observed in the $MAPbI_3$@graphite composites when the graphite amount increases, except for the composite with 0.5 wt% of graphite. The higher the graphite amount, the lower the PL peak intensity while the PL peak intensity of $MAPbI_3$@graphite 0.5 wt% remains similar to that of $MAPbI_3$ alone (Figure 9A). This may be explained by the low amount of graphite resulting in the lack of close contact with the HP.

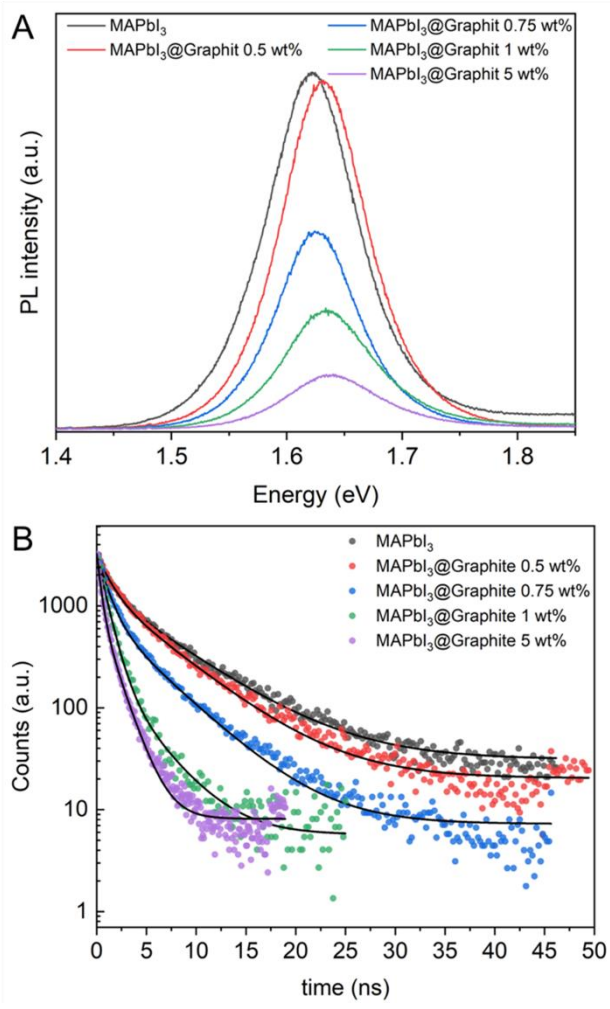

Figure 9. A) PL spectra of $MAPbI_3$ and $MAPbI_3$@Graphite as function of the graphite amount (R=40, t= 30 min) (PL excitation at 320 nm) and B) Time-resolved PL spectra of $MAPbI_3$, and $MAPbI_3$@Graphite 0.5, 0.75, 1 and 5 wt% (R=40, t= 30 min) (bi-exponential fitting).

Such a decrease in PL intensity has also been reported, for example, during PL measurements in HP and graphene heterostructures consisting of $MAPbBr_2I$ islands deposited on graphene[33] or $MAPbI_3$/graphite nanocrystals films obtained by spin coating[40] or $MAPbI_3$ spin coated on graphene layer[39] or by mixing $MAPbI_3$ with graphene quantum dots[36]. In all cases, it was ascribed to an efficient charge transfer between graphene and hybrid perovskites and would be due to interactions between hybrid perovskite and sp^2 hybridized graphene orbitales[36,39]. Kim *et al.*[81], have also observed a graphene-mediated enhanced Raman scattering in a composite consisting in $CsPbI_3$ perovskite nanorods sandwiched between layers of graphene. They noticed that the PL intensity of $CsPbI_3$ nanorods drastically decreased with increasing graphene coverage and they also attributed it to a charge transfer between graphene and $CsPbI_3$. After Zhang *et al.*[41], a carrier collection efficiency at the interface between $CH_3NH_3PbI_3$ and graphene electrode could be estimated from the PL quench: $\eta_{PL} = 1 - (I_{\text{with graphite}}/ I_{\text{without graphite}})$ where $I_{\text{with graphite}}$ and $I_{\text{without graphite}}$ indicate the PL intensities of $MAPbI_3$ with and without graphite. In our case, such carrier collection efficiency is observed to increase with the amount of graphite with values of 2.1, 44.3, 66.3 and 84.2 % for 0.5, 0.75, 1 and 5 wt% of graphite respectively.

Table 5. Band gap (UV-Vis spectra), PL peak position and time constants t_1 and t_2, obtained from bi-exponential fits of time resolved PL spectra, of mechanosynthesized $MAPbI_3$ and $MAPbI_3$@Graphite composites as a function of graphite amount for R=40 and t=30 min.

	Band gap (eV)	PL peak (eV)*	t_1(ns)**	t_2(ns)**
$MAPbI_3$	1.55	1.62	1.20	6.29
$MAPbI_3$@Graphite 0.5 wt%	1.55	1.63	1.25	5.57
$MAPbI_3$@Graphite 0.75 wt%	1.55	1.63	1.03	4.74

$MAPbI_3$@Graphite 1 wt%	1.56	1.64	0.91	3.38
$MAPbI_3$@Graphite 5 wt%	1.57	1.64	0.40	1.48

*PL peaks obtained on powders compacted in wafers, which induce a blue shift of the emission.

**The time constants t_1 and t_2 are given here for comparison with previously published results.

Time-resolved PL measurements were also performed to further investigate the influence of the graphite amount. A clear effect of graphite amount is observed on the emission decays and these results are in good agreement with the previous observed PL quenching phenomenon. A bi-exponential model has been used at first to fit the data and the obtained time constants, reported in Table 5, became shorter when the graphite amount increased with drastic differences between the composites with 0.5 and 5 wt% of graphite. The PL lifetime of $MAPbI_3$ depends on the sample's characteristics and on measurement conditions: crystal size, film thickness, substrates, etc. The time constant values obtained for the $MAPbI_3$ wafer from the bi-exponential fitting are close to those of bare $MAPbI_3$ thin films with reported values ranging from ~3 ns up to ~10 ns[57,84,85]. D'Innocenzo *et al.* [58] performed static and time resolved PL spectra on films of $MAPbI_3$ with different crystallite size and reported a lifetime of around 2 ns when the crystallite size is smaller than 250 nm. They suggested an enhancement of the non-radiative channels when the polycrystallinity increases and a higher amount of defects when the crystallite size decreases. In the composites, the crystallite size is slightly higher than that of $MAPbI_3$ but a decrease in the aggregate size with the graphite amount (Figure S7) has been noticed. Thus, the aggregate size may be a more important parameter than the crystallite size.

Nevertheless, our PL decay data, for the composite samples, did not fit well by a monomolecular model, even a multi-exponential function can hardly fit them, as seen when plotted on a log-scale on the y-axis (Figure 9B). Indeed, the curves clearly displayed that, when

graphite is introduced, the decay slowed down with time. Thus, to further understand the lifetime quenching, the study of PL dynamic was carried out by applying another PL decay curve-fitting model: the bimolecular recombination model, which is more simplified compared with the bi-exponential one. In this process, the time-dependant excitation density can be expressed by the following function[86–89]: $\tilde{n}(t) = \frac{\tilde{n}(0)}{1+\tilde{n}(0)\beta t}$ with $\tilde{n}(t)$ representing the time dependant charge carrier density and β representing the bimolecular recombination rate. As the time-resolved PL intensity is proportional to the square of photocarrier density, the PL decay curve can be fitted by the expression shown below which is characterized by a slope of 2 under the log-log plotting scale: $I = \frac{a}{(1+bt)^2}$. The fitting also with a bimolecular model of mechanosynthesized $MAPbI_3$ decay, could be a signature that the prevailing process is dominated by free carriers, as the exciton binding energy is very low in $MAPbI_3$ at room temperature[87]. The fitting results of the time-resolved PL curves of the MS $MAPbI_3$ alone and of the composite with 0.5 wt% graphite matched well with the bimolecular kinetic model, giving a slope value of 2 (Figure 10). For the ones with a graphite amount equal or superior to 0.75 wt%, the decays continue to be fitted by a power law: $I = \frac{a}{(1+bt)^c}$, with only an increase of the slopes in the linear part in the log-log plots (Figure 10). Thus, the $MAPbI_3$ kinetics fits with a recombination process with collisions within the free charge carriers, notably electrons and holes, instead of a radiative recombination that would give rise to a monomolecular exponential decay. Such results showed that only the perovskite phase was involved in the recombination process when the graphite amount was 0 and 0.5 wt% and that the graphite started to participate in PL dynamic when its amount is higher than this threshold value of 0.5 wt% as the power factor c in the power law started to differ from 2. Therefore, the interactions between $MAPbI_3$ and graphite in composites (when the graphite amount is higher than 0.5 wt%) are responsible of the observed static PL quenching and PL decay.

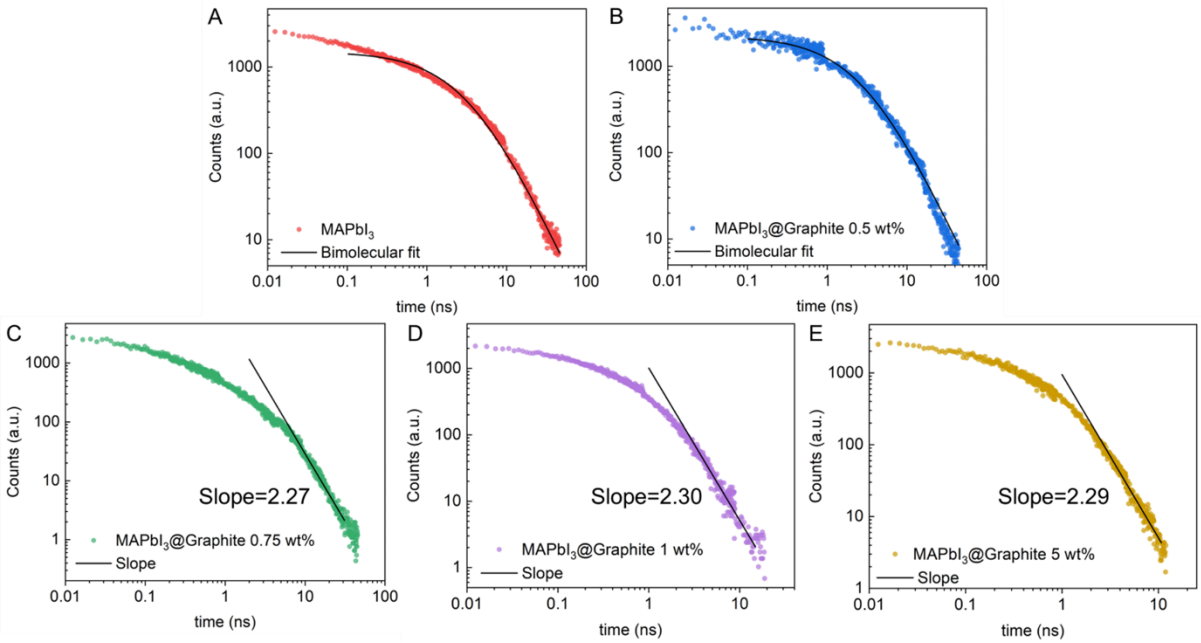

Figure 10. PL decay curve fitting with the bimolecular kinetic model of $MAPbI_3$, and $MAPbI_3$@graphite 0.5, 0.75, 1 and 5 wt% (R=40, t= 30 min).

The graphite enhancement RAMAN scattering and the decrease in PL intensity with the presence of graphene pointed to a charge transfer between graphite and $MAPbI_3$ [13,16,36,39,40,90]. Thus, the slopes increase in the linear part of the decays related to the composites, with graphite amount higher than 0.5 wt%, in the log-log is expected to be due to an effective charge trapping at interfaces when enough graphite is introduced. Indeed, the presence of graphite should induce a modification of the Coulomb interactions, which should favour the presence/attraction of charge carriers close to the graphite-$MAPbI_3$ interfaces. That would be in agreement with the increase in carrier collection efficiency with the increase in graphite amount deduced from PL measurements. As the graphite sheets are evenly distributed all along the composites through the ultimate mixing provided by the mechanosynthesis process, $MAPbI_3$ is in very close contact with graphite and thus many strong interfaces between $MAPbI_3$ and graphite are created, which should favour the presence of higher amount of carriers and then a charge carrier trapping. This

is also supported by the fact that graphite/graphene has often been reported to favour the charge separation.[33,39,46]

3. Transport measurement and X-Ray detection performance

We have then compared the transport properties of a $MAPbI_3$ wafer and a composite wafer with 1 wt% graphite (Figure 11A). The 700 µm-thick $MAPbI_3$ wafer with a diameter of 7 mm presented a very high sheet resistance of around 12 MΩ/□ at 340 K, implying an even higher value at room temperature given the insulating character of the transport properties[91]. Interestingly, the same measurement for a composite wafer with the same nominal dimension rendered a decrease of the overall sheet resistance of a factor three, indicating a strong interaction between the graphite and perovskite phases.

Some preliminary tests on the X-Ray detection performance were also carried out. X-Ray induced photocurrent measurement is a useful tool to assess the charge transport in perovskite materials, as the photocurrent intensity is directly related to the *mobility-lifetime product* µτ of the charge carriers. Besides, due to the penetrative nature of the X-Ray radiation that generates charge carriers throughout the bulk, this type of characterization is less sensitive than UV-Visible light-induced photocurrent to surface states and defects. Hence, we fabricated Cr/Perovskite/Cr devices based on $MAPbI_3$ and composite (1%wt) wafers. Chromium electrodes were shown in previous works to provide reliable electrical contacts to $MAPbI_3$ wafers[92,93]. Figure 11B showed that the compacted $MAPbI_3$ device processes a direct X-Ray to current conversion property, while this photocurrent response is not noticed on the composite wafer. We attributed the loss of device response to X-Ray to the orbital interactions between graphite and $MAPbI_3$, resulting in the interference of photogenerated charge transport and recombination process under the exposure to X-Ray. The irreversible loss of the photogenerated charges drastically quenched the photocurrent response for the 1%wt graphite sample. It should be noted that the wafers were irradiated with rather high energy photons (mean energy 50 keV),

hence generating charge carrier in all the volume of the 800-µm thick wafer (~90% of incident X-Rays are absorbed). We attributed thus the lack of photocurrent response to a bulk phenomenon rather than recombination at the surface of the wafers, which is in accordance with the intimate distribution of graphite particles in the wafer (see Figure 6). Notably, no photocurrent was measured for the 1%wt graphite wafer at negative bias nor at positive bias, suggesting that both types of charge carriers (electrons and holes) are symmetrically trapped and/or recombined during the irradiation process.

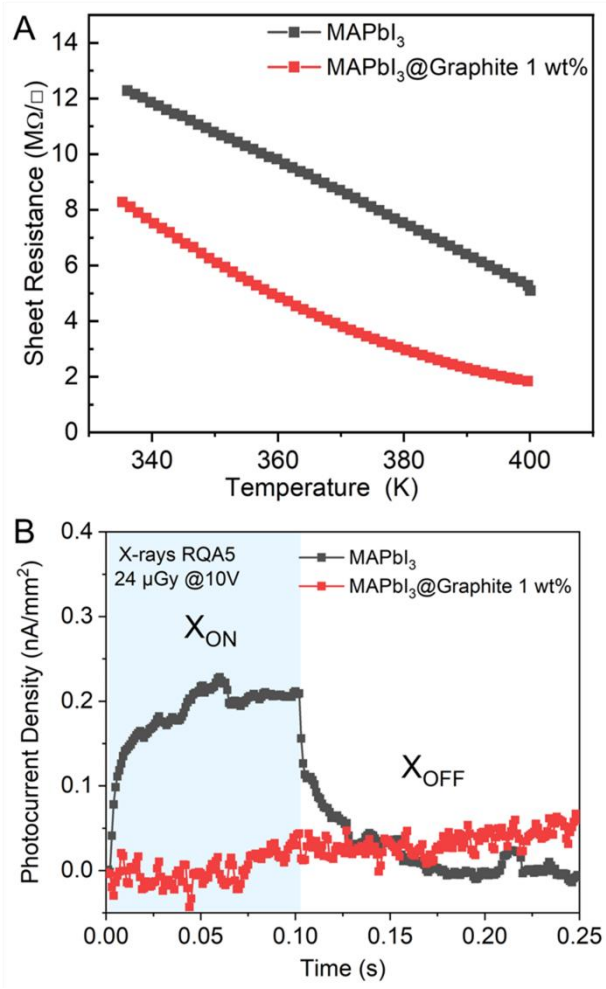

Figure 11. A) Sheet resistance as a function of temperature of mechanosynthesized $MAPbI_3$ wafer and the composite wafer with 1 wt% of graphite B) photocurrent response under X-Ray exposure and a 10 V bias.

4. Photodetection measurements

Photodetection measurements have been performed by putting two tungsten tips in contact with the surface and registering I-V curves under different irradiance starting from 1SUN AM1.5G conditions and the photoresponsivity as function of the wavelength. The I-V curves under dark and then different illumination conditions between -5 and 5 V show that the dark current in mechanosynthesized $MAPbI_3$, between 10^{-8}-10^{-7} A (Figure 12A), is slightly higher but in the range of the reported ones for polycrystalline samples [16,94,95]. The minimum current in Figure 12A is not at 0V but -1V and such positioning has already been observed during measurement in dark conditions and attributed to polycrystallinity and/or defects[96]. Under different illumination powers (1 SUN= 100 mW/cm^2), the minimum current shift is always observed and very slight photocurrent was noticed in I-V curves between -5 V and 5 V: the current at -5 V bias was around 1.8×10^{-7} A and around $2.7\text{x}10^{-8}$ A at – 2V bias (Figure S9A). In fact, a more significant change in the current is noticed between the dark and the illumination at voltage higher than 8V as seen in Figure S10. Photoresponsivity curves at different wavelengths have been thus registered at 10 V and evidenced a quite low photoresponsivity between 10^{-4} and 10^{-2} A/W in the UV-Vis wavelength range (Figure 13A) in comparison to published values[16]. Similar results were obtained with the composite with 1 wt % graphene.

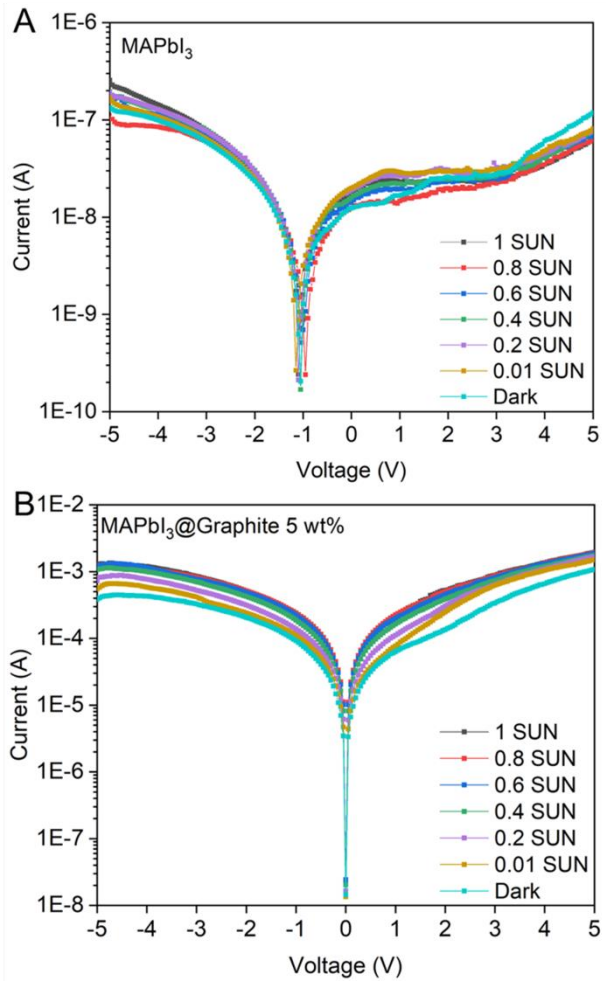

Figure 12. I-V curves under dark and different irradiance of mechanosynthezised A) $MAPbI_3$ and B) $MAPbI_3$@Graphite 5 wt%

By contrast, when 5 wt% of graphite is introduced, the dark current increases due to the presence of conductive graphite[40,42] (around 3.4×10^{-4} A at 3 V and 1.1×10^{-3} at 5 V) and experiments under higher voltage bias up to 15 V show a continuous increase of photocurrent with the voltage bias in comparison with $MAPbI_3$. There is no shift of the minimum current as observed with MS $MAPbI_3$ (Figure 12B). It stays centred at 0 V and a photocurrent is noticed as a function of the illumination power: at 3 V: 3.4×10^{-4} A under dark and 8.9×10^{-4} A under 1SUN; at 5 V: 1.1×10^{-3} A under dark and 1.9×10^{-3} A under 1 SUN. This last value is nearly reached already with an irradiance of 0.6 SUN (60 mW cm^{-2}) and is of 1.5×10^{-3} A at 1 mW cm^{-2} (0.01 SUN) (Figures 12A and S11). Wang *et al.*[40] with a mixture of HP with 0.1% graphite

nanocrystals at 5 V under light illumination at 500 nm with an intensity of 0.2 mW cm^{-2} obtained a current of 2.2×10^{-8} A and 4.8×10^{-8} A with $MAPbI_3$ and the composite respectively. Under light irradiation at 520 nm with an intensity of 3.2 mW cm^{-2}, the $MAPbI_3$/rGO photodetector of He *et al.*[90] exhibits a photocurrent of 28.56×10^{-9} A larger than that of neat $MAPbI_3$ (4.47×10^{-9} A).

Photoresponsivity curve at different wavelength in Figure 13A demonstrated further that the composite is efficient between 300 and 1200 nm, which is the range of the measurement setup. This result is quite interesting as composites of graphite and $MAPbI_3$ are often reported to be efficient only below 800 nm[16,39] but we may notice that, in published results, the devices were either in bilayer configuration or the amount of graphene was lower. The effective quantum efficiency (EQE) curves in Figure 13B confirmed the higher performance of the composite in comparison with $MAPbI_3$ alone with a mean EQE value around 10^6 %, much higher than the $MAPbI_3$ one around 6 %. One may further notice that the EQE is higher in the UV wavelength range (300-400 nm) around 10^7 % and around 10 % for the composite and $MAPbI_3$ respectively as often reported for $MAPbI_3$ and composites with graphite.

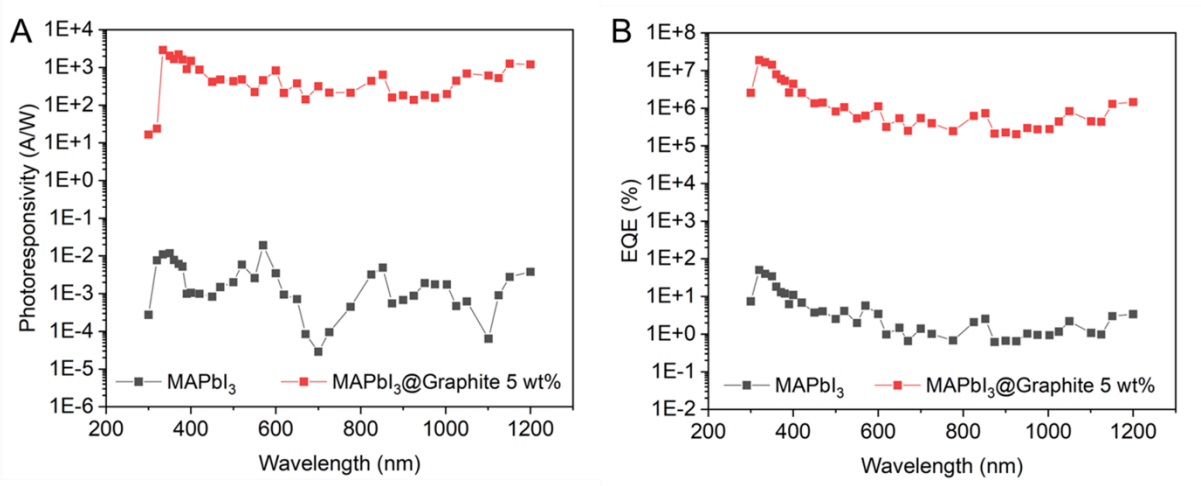

Figure 13. A) Photoresponsivity and B) effective quantum efficiency vs. wavelengths for mechanosynthesized $MAPbI_3$ and $MAPbI_3$@Graphite 5 wt% at 10V bias

A photoconductivity around 0.5 A/W and EQE around 90% at 400 nm were reported by Lee *et al.*[39] for a layered/stacked perovskite-graphene hybrid photodetector and their best results are a photoresponsivity and EQE of 180 A/W and 5×10^4 % at an illumination power of 1 μW and applied bias of 0.1 V, respectively. Spina *et al.*[46] with $MAPbI_3$ nanowires deposited on graphene reported a photoresponsivity of 2.6×10^6 A/W at $V_D = 10$ mV and 3 pW. Wang *et al.*[33] observed a responsivity of $\approx 6.0 \times 10^5$ A/W in graphene sheets bearing isolated $MAPbI_3$ islands based phototransistor ($V_{DS} = 3$ V) while illuminated at 405 nm with a power of 1.052 nW. In our measurement conditions: we obtained, at 400 nm with a light power of 330 nW, a photoconductivity of 1.5×10^3 A/W and EQE of around 4.4×10^6 % for the composite sample (Figure 13). The photoresponsivity is observed to decrease when the irradiance increases[33,40,46] : ~0.02 A/W at 1 mW/cm^2 for Wang *et al.*[40] and the responsivity decreases with thinner thickness of samples[40,97]. Higher photoresponsivity can be achieved when decreasing the illumination power or increasing the bias voltage[33]. Considering these observations, one may suggest that our results are quite encouraging (even if the measurements are not realized in the same conditions) and that the homogeneous mixture of graphite and $MAPbI_3$ with strong interactions obtained by mechanosynthesis are promising for photodetection.

To further confirm the importance of the mechanosynthesis process to obtain a composite with good photodetection performance, a "blank" sample was prepared by mixing manually the mechanosynthesized $MAPbI_3$ with 5 wt% raw graphite and then compressing the so mixed powders into wafer. The photodetection results showed that no illumination condition-dependent photocurrent response was observed on the wafer obtained with the powders mixture (Figure S9B and S9C). Indeed, the detected current value and the device response of the simple mixture wafer are very similar to those of the graphite alone suggesting a strong percolation of graphite in the mixture sample. This photodetection test demonstrates that the

mechanosynthesis approach played an important role to achieve the ultimate mixture between graphite and $MAPbI_3$ and to provide active interfaces improving the photodetection performance.

All these results clearly evidence that the addition of only 5 wt% of graphite during the mechanosynthesis of $MAPbI_3$ provided a composite with an effective microstructure that greatly improved its photodetection performance. However, a good photodetector should be also a good X-Ray detector and the performances are very different here. One may explain such differences by the different irradiation conditions. Indeed, X-Ray detection affects the bulk when the photodetection affects mainly the surface of composite. Therefore, these different irradiation conditions and surface effects may result in very different photogenerated charge densities, as the photogenerated charge carriers are created across the detector thickness under X-Ray exposure, and only in the first hundreds of nanometer under light exposure due to the different penetration ability of X-Ray and normal light exposures. In addition, it should be noted that the corresponding power density of the X-ray beam used in this work is only 1 $\mu W/cm^2$, and is as high as 100 mW/cm^2 for photodetection. It is not surprising that these highly different charge generation conditions result in highly different device behaviour and should explain the better performance in photodetection of our composite by comparison with X-Ray detection.

The high photoresponsivity and EQE values of our composite in our measurement conditions confirm that a charge transfer occurs between $MAPbI_3$ and graphite as suggested by Raman spectroscopy and PL measurements. The highly polycrystalline nature of mechanosynthesized $MAPbI_3$ and also certainly some defects should explain that the photodetection efficiency of MS $MAPbI_3$ is affected under illumination. The addition/presence of graphite, which is homogenously distributed within the composites with strong interfaces thanks to the mechanosynthesis process and which modifies the coulomb interactions, allows reducing, in our photodetection measurement conditions, the negative effect of the polycrystallinity and

defects and favoring the charge carrier "attraction" and separation. Most of time such high EQE value, exceeding 100%, as observed in our composite sample, are explained by a photoconductive gain[13,16,98,99]. Several mechanisms may explain this gain but the most reported mechanism is the trapping of one type of charge carrier and the other one is multiplied via injection from the contact electrodes thus contributing even more to the photoconductivity. For example, it has been reported that the quenching of PL, when graphene is added, would support that the recombination of photoexcited electron-hole pairs in the hybrid perovskite is efficiently reduced and the charge transfer mechanism is that the electrons transfer from graphene to hybrid perovskite to fill its empty states in the valence band and the trapped electrons from the graphite exhibited effective photogating effects[16,39]. Thus, the photoexcited electrons remained in the perovskite conduction band, improving the photodetection current. Another explanation is that the photogenerated holes in the perovskite are transferred to the graphite sheet through the interface, leaving the electrons trapped in perovskites and thus the circulation of positive charges increases the photoconductivity and the gain[33] (Figure 14). Therefore, the detection efficiency/performance with the composite, is certainly due to surface effects and to the strong interfaces between graphite and $MAPbI_3$ (generated by the mechanosynthesis process), which leads to an improved charge transfer and amplification of the photocurrent. Other measurements will be needed to further identify the trapped charge carrier type related to the rise of the photoresponsivity as well as to perform measurements in other photodetection device configurations. Furthermore, the same characterizations were performed on the composite, after 7 weeks of storage in a close container without sealing, to follow up the impact of ageing on the composite properties. No degradation products were identified in XRD pattern (Figure S12A). The photodetection measurements gave similar I-V response as the fresh sample under different illumination condition (0.01 to 1 SUN) between -5 and 5V (Figure S12B). The photoresponsivity and EQE were also very similar to the fresh composite sample (Figure S13).

These results showed a good stability of the solvent-free mechanosynthesized $MAPbI_3$@graphite composite powders.

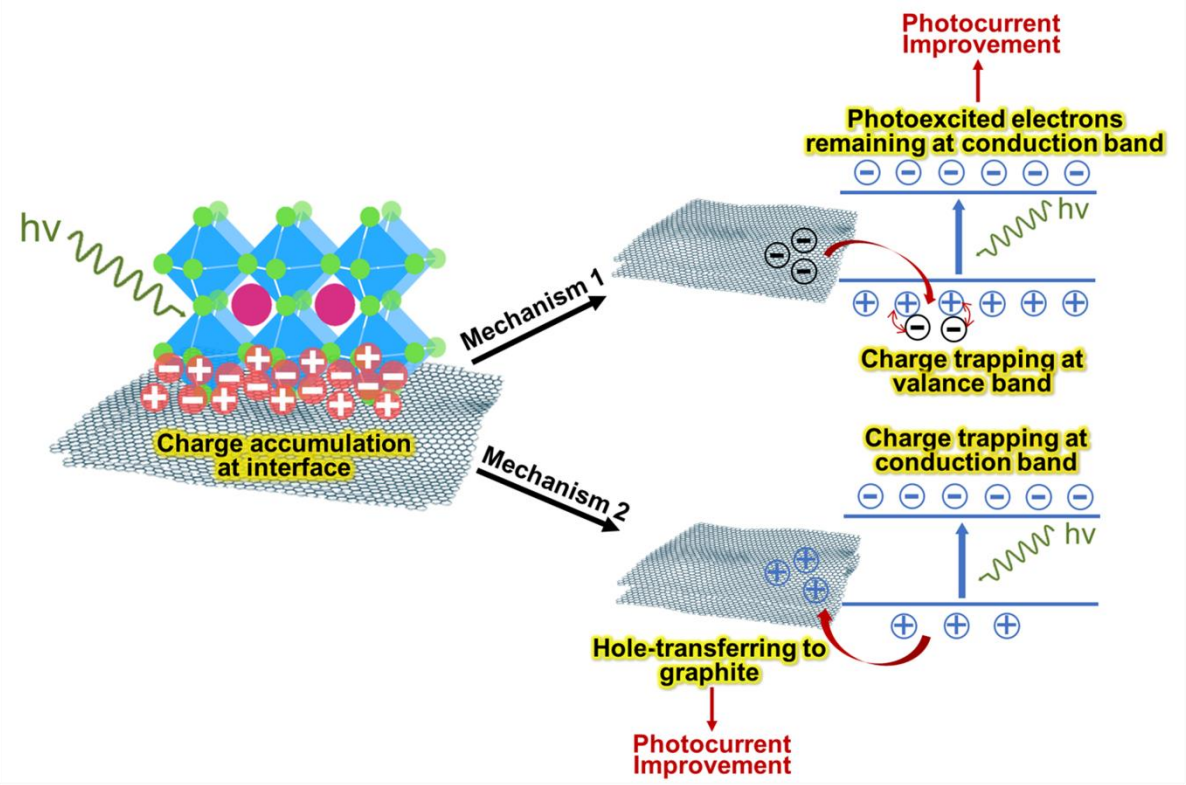

Figure 14. Schematic representation of discussed possible charge transfer mechanisms in $MAPbI_3$@Graphite 5 wt% composite

Conclusion

The mechanosynthesis of the hybrid perovskite, $MAPbI_3$ and of composites $MAPbI_3$@graphite with different graphite amounts has been studied in a planetary ball-mill. The mechanosynthesis conditions of $MAPbI_3$ have been optimized (R=40 and grinding time of 30 min) to introduce low amount of defects and have been shown to conduct to lattice parameters, band gap and PL properties in agreement with reported values for $MAPbI_3$ synthesis from chemical approaches. XRD analysis, HRTEM and in situ HRTEM as a function of temperature revealed that the as-ground powders display a certain mosaicity, i.e., the nanograins in aggregates shared common crystallographic orientations. These MS conditions

were found suitable to mechanosynthesize the composites, which presented the same microstructural characteristics as the MS $MAPbI_3$. SEM and HRTEM evidenced a close contact between $MAPbI_3$ and few-layer graphite.

The Raman spectroscopy, evidencing a graphite-enhanced Raman scattering, and the characterization of opto-electronic properties by steady-state and time resolved PL measurements as well as their properties as X-Ray and photo-detectors allowed concluding on an improved charge transfer and amplification of the photocurrent in the composites with graphite, which agree with the mechanism of trapping of one type of charge carrier. The composite with 5 wt% of graphite was shown to exhibit a high photoconductive gain very promising for photodetection applications.

We showed here that the green and easy to handle mechanosynthesis process leads to homogeneous composites with strong interactions between graphite and $MAPbI_3$: the encouraging results just based on a simple compacted wafer of mechanosynthesized composite powders gives rise to novel design/fabrication of photodetectors built from powders that could be easily synthesized in large amounts. Further enhancements of photodetector performance could be expected by improving the interface between the composite and electrodes, testing different photodetector device configurations and better understanding the charge transfer mechanism. These results pave the way for exploiting perovskites-graphite composites photodetectors based on mechanosynthesized powders.

Supporting information. XRD pattern of reactant mixture after milling for 10 min and R=30 and evolution of $R_{PbI2/MAPbI3}$ with grinding time with R= 30; PL and UV-vis spectra of mechanosynthesized powders at R=40, t=30min; SEM images at low magnification and at higher magnification of ground powders and of a cross-section of a wafer of compacted powder ground with R=40 for 30min; XRD patterns of ground $MAPbI_3$ at 25°C and 70°C and characteristic XRD peaks changes in the thermo X-Ray diffraction patterns of ground $MAPbI_3$

at different temperature; XRD patterns of $MAPbI_3$ composites with 5 wt%, 1 wt%, 0.75 wt% and 0.5 wt% of graphite, mechanosynthesized $MAPbI_3$ and $MAPbI_3$ simulation; SEM images in COMPO mode of surface of wafers of $MAPbI_3$, $MAPbI_3$@Graphite 0.5 wt% graphite, $MAPbI_3$@Graphite 0.75 wt% graphite, $MAPbI_3$@Graphite 1 wt% graphite and $MAPbI_3$@Graphite 5 wt% graphite; Raman spectra of graphite milled graphite and $MAPbI_3$@Graphite composites of different graphite amounts; photocurrent of $MAPbI_3$ and $MAPbI_3$@Graphite 5 wt% wafer under dark and different irradiance at -5V bias; I-V curves of $MAPbI_3$ under dark and 1 SUN AM1.5G illumination between -15 and 15V and I-V curves of $MAPBI_3$@Graphite 5 wt% wafer under dark and different irradiance between -5 and 5V.

Corresponding authors

Sylvie Begin-Colin, sylvie.begin@unistra.fr

Clément Sanchez, clement.sanchez@sorbonne-universite.fr

Dominique Begin, dominique.begin@unistra.fr

Author Contributions.

The manuscript was written through contributions of all authors. All authors have given approval to the final version of the manuscript.

Funding Sources.

We thank the CNRS, University of Strasbourg, and the French Ministry of Research (fellowship to Yihui Cai) for financial support. This project received funding from National Institute of Physics of CNRS (AAP Tremplin@INP). This work has received funding from the European Union's Horizon 2020 research and innovation program under the Photonics Public Private Partnership (www.photonics21.org) with the project PEROXIS under Grant Agreement No.

871336. The authors thank GDR HPERO for its scientific activities and its mobility funding to visit CEA LETI.

ACKNOWLEDGMENT

The authors thank the XRD, SEM and TEM platforms of the IPCMS and ICPEES. Pr Frédéric Antoni at ICUBE is thanked for Raman spectroscopy facilities as well as Cédric Leuvrey and Marc Lenertz for SEM and XRD analyses respectively.

ABBREVIATIONS

HP, hybrid perovskites; $MAPbI_3$, $CH_3NH_3PbI_3$; HRTEM, high resolution transmission electron microscopy; MS, mechanosynthesized; PL, Photoluminescence; LED, light emitting diodes; FRET, Förster resonance energy transfer; MAI, $CH_3NH_3I_2$; XRD, X-Ray diffraction; UV, ultra violet; Vis, visible: TEM, Transmission electron microscopy; SAED, selected area electron diffraction; SEM, Scanning Electronic Microscopy; FFT, fast Fourier transform.

References

(1) Green, M. A.; Dunlop, E. D.; Hohl-Ebinger, J.; Kopidakis, N.; Hao, X. Solar Cell Efficiency Tables (Version 59). *Prog Photovolt Res Appl* **2022**, *30* (1), 3–12. https://doi.org/10.1002/pip.3506.

(2) De Wolf, S.; Holovsky, J.; Moon, S.-J.; Löper, P.; Niesen, B.; Ledinsky, M.; Haug, F.-J.; Yum, J.-H.; Ballif, C. Organometallic Halide Perovskites: Sharp Optical Absorption Edge and Its Relation to Photovoltaic Performance. *J. Phys. Chem. Lett.* **2014**, *5* (6), 1035–1039. https://doi.org/10.1021/jz500279b.

(3) Green, M. A.; Ho-Baillie, A.; Snaith, H. J. The Emergence of Perovskite Solar Cells. *Nature Photon* **2014**, *8* (7), 506–514. https://doi.org/10.1038/nphoton.2014.134.

(4) Li, W.; Wang, Z.; Deschler, F.; Gao, S.; Friend, R. H.; Cheetham, A. K. Chemically Diverse and Multifunctional Hybrid Organic–Inorganic Perovskites. *Nat Rev Mater* **2017**, *2* (3), 16099. https://doi.org/10.1038/natrevmats.2016.99.

(5) Kovalenko, M. V.; Protesescu, L.; Bodnarchuk, M. I. Properties and Potential Optoelectronic Applications of Lead Halide Perovskite Nanocrystals. *Science* **2017**, *358* (6364), 745–750. https://doi.org/10.1126/science.aam7093.

(6) Xing, G.; Mathews, N.; Lim, S. S.; Yantara, N.; Liu, X.; Sabba, D.; Grätzel, M.; Mhaisalkar, S.; Sum, T. C. Low-Temperature Solution-Processed Wavelength-Tunable Perovskites for Lasing. *Nature Mater* **2014**, *13* (5), 476–480. https://doi.org/10.1038/nmat3911.

(7) An, M. N.; Park, S.; Brescia, R.; Lutfullin, M.; Sinatra, L.; Bakr, O. M.; De Trizio, L.; Manna, L. Low-Temperature Molten Salts Synthesis: $CsPbBr_3$ Nanocrystals with High Photoluminescence Emission Buried in Mesoporous SiO_2. *ACS Energy Lett.* **2021**, 900–907. https://doi.org/10.1021/acsenergylett.1c00052.

(8) Dong, G.-X.; Zhang, W.; Mu, Y.-F.; Su, K.; Zhang, M.; Lu, T.-B. A Halide Perovskite as a Catalyst to Simultaneously Achieve Efficient Photocatalytic CO_2 Reduction and Methanol Oxidation. *Chem. Commun.* **2020**, *56* (34), 4664–4667. https://doi.org/10.1039/D0CC01176B.

(9) Zhu, X.; Lin, Y.; San Martin, J.; Sun, Y.; Zhu, D.; Yan, Y. Lead Halide Perovskites for Photocatalytic Organic Synthesis. *Nat Commun* **2019**, *10* (1), 2843. https://doi.org/10.1038/s41467-019-10634-x.

(10) Huang, H.; Pradhan, B.; Hofkens, J.; Roeffaers, M. B. J.; Steele, J. A. Solar-Driven Metal Halide Perovskite Photocatalysis: Design, Stability, and Performance. *ACS Energy Lett.* **2020**, *5* (4), 1107–1123. https://doi.org/10.1021/acsenergylett.0c00058.

(11) Tian, W.; Zhou, H.; Li, L. Hybrid Organic-Inorganic Perovskite Photodetectors. *Small* **2017**, *13* (41), 1702107. https://doi.org/10.1002/smll.201702107.

(12) Wang, X.; Li, M.; Zhang, B.; Wang, H.; Zhao, Y.; Wang, B. Recent Progress in Organometal Halide Perovskite Photodetectors. *Organic Electronics* **2018**, *52*, 172–183. https://doi.org/10.1016/j.orgel.2017.10.027.

(13) Ghosh, J.; Giri, P. K. Recent Advances in Perovskite/2D Materials Based Hybrid Photodetectors. *J. Phys. Mater.* **2021**, *4* (3), 032008. https://doi.org/10.1088/2515-7639/abf544.

(14) Mayén Guillén, J.; Lédée, F.; Baussens, O.; Chapran, M.; Lemercier, T.; Verilhac, J.-M.; Gros-Daillon, E.; Ibanez, A.; Zaccaro, J. $MAPb(Br_{1-x}Cl_x)_3$ Hybrid Perovskite Materials for Direct X-Ray Detection. *ACS Appl. Electron. Mater.* **2023**, acsaelm.3c00114. https://doi.org/10.1021/acsaelm.3c00114.

(15) Basiricò, L.; Ciavatti, A.; Fraboni, B. Solution-Grown Organic and Perovskite X-Ray Detectors: A New Paradigm for the Direct Detection of Ionizing Radiation. *Adv. Mater. Technol.* **2021**, *6* (1), 2000475. https://doi.org/10.1002/admt.202000475.
(16) Wang, H.; Kim, D. H. Perovskite-Based Photodetectors: Materials and Devices. *Chem. Soc. Rev.* **2017**, *46* (17), 5204–5236. https://doi.org/10.1039/C6CS00896H.
(17) Ahmadi, M.; Wu, T.; Hu, B. A Review on Organic–Inorganic Halide Perovskite Photodetectors: Device Engineering and Fundamental Physics. *Adv. Mater.* **2017**, *29* (41), 1605242. https://doi.org/10.1002/adma.201605242.
(18) Krishna, A.; Gottis, S.; Nazeeruddin, M. K.; Sauvage, F. Mixed Dimensional 2D/3D Hybrid Perovskite Absorbers: The Future of Perovskite Solar Cells? *Adv. Funct. Mater.* **2019**, *29* (8), 1806482. https://doi.org/10.1002/adfm.201806482.
(19) Arabpour Roghabadi, F.; Alidaei, M.; Mousavi, S. M.; Ashjari, T.; Tehrani, A. S.; Ahmadi, V.; Sadrameli, S. M. Stability Progress of Perovskite Solar Cells Dependent on the Crystalline Structure: From 3D ABX $_3$ to 2D Ruddlesden–Popper Perovskite Absorbers. *J. Mater. Chem. A* **2019**, *7* (11), 5898–5933. https://doi.org/10.1039/C8TA10444A.
(20) Leguy, A. M. A.; Hu, Y.; Campoy-Quiles, M.; Alonso, M. I.; Weber, O. J.; Azarhoosh, P.; van Schilfgaarde, M.; Weller, M. T.; Bein, T.; Nelson, J.; Docampo, P.; Barnes, P. R. F. Reversible Hydration of CH $_3$ NH $_3$ PbI $_3$ in Films, Single Crystals, and Solar Cells. *Chem. Mater.* **2015**, *27* (9), 3397–3407. https://doi.org/10.1021/acs.chemmater.5b00660.
(21) Zhang, Y.; Seo, S.; Lim, S. Y.; Kim, Y.; Kim, S.-G.; Lee, D.-K.; Lee, S.-H.; Shin, H.; Cheong, H.; Park, N.-G. Achieving Reproducible and High-Efficiency (>21%) Perovskite Solar Cells with a Presynthesized FAPbI $_3$ Powder. *ACS Energy Lett.* **2020**, *5* (2), 360–366. https://doi.org/10.1021/acsenergylett.9b02348.
(22) Leupold, N.; Panzer, F. Recent Advances and Perspectives on Powder-Based Halide Perovskite Film Processing. *Adv. Funct. Mater.* **2021**, *31* (14), 2007350. https://doi.org/10.1002/adfm.202007350.
(23) Jodlowski, A. D.; Yépez, A.; Luque, R.; de Miguel, G. Benign-by-Design Solventless Mechanochemical Synthesis of Three-, Two-, and One-Dimensional Hybrid Perovskites. *Angew. Chem. Int. Ed.* **2016**, *55* (48), 14972–14977. https://doi.org/10.1002/anie.201607397.
(24) Hong, Z.; Tan, D.; John, R. A.; Tay, Y. K. E.; Ho, Y. K. T.; Zhao, X.; Sum, T. C.; Mathews, N.; García, F.; Soo, H. S. Completely Solvent-Free Protocols to Access Phase-Pure, Metastable Metal Halide Perovskites and Functional Photodetectors from the Precursor Salts. *iScience* **2019**, *16*, 312–325. https://doi.org/10.1016/j.isci.2019.05.042.
(25) Ma, Y.; Liu, Y.; Shin, I.; Hwang, I.-W.; Jung, Y. K.; Jeong, J. H.; Park, S. H.; Kim, K. H. Understanding and Tailoring Grain Growth of Lead-Halide Perovskite for Solar Cell Application. *ACS Appl. Mater. Interfaces* **2017**, *9* (39), 33925–33933. https://doi.org/10.1021/acsami.7b10022.
(26) Stoumpos, C. C.; Malliakas, C. D.; Kanatzidis, M. G. Semiconducting Tin and Lead Iodide Perovskites with Organic Cations: Phase Transitions, High Mobilities, and Near-Infrared Photoluminescent Properties. *Inorg. Chem.* **2013**, *52* (15), 9019–9038. https://doi.org/10.1021/ic401215x.
(27) Prochowicz, D.; Saski, M.; Yadav, P.; Grätzel, M.; Lewiński, J. Mechanoperovskites for Photovoltaic Applications: Preparation, Characterization, and Device Fabrication. *Acc. Chem. Res.* **2019**, *52* (11), 3233–3243. https://doi.org/10.1021/acs.accounts.9b00454.
(28) Palazon, F.; El Ajjouri, Y.; Bolink, H. J. Making by Grinding: Mechanochemistry Boosts the Development of Halide Perovskites and Other Multinary Metal Halides. *Adv. Energy Mater.* **2020**, *10* (13), 1902499. https://doi.org/10.1002/aenm.201902499.

(29) Prochowicz, D.; Runjhun, R.; Tavakoli, M. M.; Yadav, P.; Saski, M.; Alanazi, A. Q.; Kubicki, D. J.; Kaszkur, Z.; Zakeeruddin, S. M.; Lewiński, J.; Grätzel, M. Engineering of Perovskite Materials Based on Formamidinium and Cesium Hybridization for High-Efficiency Solar Cells. *Chem. Mater.* **2019**, *31* (5), 1620–1627. https://doi.org/10.1021/acs.chemmater.8b04871.
(30) Prochowicz, D.; Franckevičius, M.; Cieślak, A. M.; Zakeeruddin, S. M.; Grätzel, M.; Lewiński, J. Mechanosynthesis of the Hybrid Perovskite $CH_3NH_3PbI_3$: Characterization and the Corresponding Solar Cell Efficiency. *J. Mater. Chem. A* **2015**, *3* (41), 20772–20777. https://doi.org/10.1039/C5TA04904K.
(31) Prochowicz, D.; Yadav, P.; Saliba, M.; Saski, M.; Zakeeruddin, S. M.; Lewiński, J.; Grätzel, M. Mechanosynthesis of Pure Phase Mixed-Cation $MA_xFA_{1-x}PbI_3$ Hybrid Perovskites: Photovoltaic Performance and Electrochemical Properties. *Sustainable Energy Fuels* **2017**, *1* (4), 689–693. https://doi.org/10.1039/C7SE00094D.
(32) Fagiolari, L.; Bella, F. Carbon-Based Materials for Stable, Cheaper and Large-Scale Processable Perovskite Solar Cells. *Energy Environ. Sci.* **2019**, *12* (12), 3437–3472. https://doi.org/10.1039/C9EE02115A.
(33) Wang, Y.; Zhang, Y.; Lu, Y.; Xu, W.; Mu, H.; Chen, C.; Qiao, H.; Song, J.; Li, S.; Sun, B.; Cheng, Y.-B.; Bao, Q. Hybrid Graphene-Perovskite Phototransistors with Ultrahigh Responsivity and Gain. *Advanced Optical Materials* **2015**, *3* (10), 1389–1396. https://doi.org/10.1002/adom.201500150.
(34) Niazi, Z.; Hagfeldt, A.; Goharshadi, E. K. Recent Progress on the Use of Graphene-Based Nanomaterials in Perovskite Solar Cells. *J. Mater. Chem. A* **2023**, *11* (13), 6659–6687. https://doi.org/10.1039/D2TA09985C.
(35) Bouclé, J.; Herlin-Boime, N. The Benefits of Graphene for Hybrid Perovskite Solar Cells. *Synthetic Metals* **2016**, *222*, 3–16. https://doi.org/10.1016/j.synthmet.2016.03.030.
(36) Zhu, Z.; Ma, J.; Wang, Z.; Mu, C.; Fan, Z.; Du, L.; Bai, Y.; Fan, L.; Yan, H.; Phillips, D. L.; Yang, S. Efficiency Enhancement of Perovskite Solar Cells through Fast Electron Extraction: The Role of Graphene Quantum Dots. *J. Am. Chem. Soc.* **2014**, *136* (10), 3760–3763. https://doi.org/10.1021/ja4132246.
(37) Volonakis, G.; Giustino, F. Interfaces Between Graphene-Related Materials and $MAPbI_3$: Insights from First-Principles. *Adv. Mater. Interfaces* **2018**, *5* (22), 1800496. https://doi.org/10.1002/admi.201800496.
(38) Duan, M.; Rong, Y.; Mei, A.; Hu, Y.; Sheng, Y.; Guan, Y.; Han, H. Efficient Hole-Conductor-Free, Fully Printable Mesoscopic Perovskite Solar Cells with Carbon Electrode Based on Ultrathin Graphite. *Carbon* **2017**, *120*, 71–76. https://doi.org/10.1016/j.carbon.2017.05.027.
(39) Lee, Y.; Kwon, J.; Hwang, E.; Ra, C.-H.; Yoo, W. J.; Ahn, J.-H.; Park, J. H.; Cho, J. H. High-Performance Perovskite-Graphene Hybrid Photodetector. *Adv. Mater.* **2015**, *27* (1), 41–46. https://doi.org/10.1002/adma.201402271.
(40) Wang, Y.; Xia, Z.; Du, S.; Yuan, F.; Li, Z.; Li, Z.; Dai, Q.; Wang, H.; Luo, S.; Zhang, S.; Zhou, H. Solution-Processed Photodetectors Based on Organic–Inorganic Hybrid Perovskite and Nanocrystalline Graphite. *Nanotechnology* **2016**, *27* (17), 175201. https://doi.org/10.1088/0957-4484/27/17/175201.
(41) Zhang, J.; Hong, H.; Zhang, J.; Wu, C.; Peng, H.; Liu, K.; Meng, S. Unravelling a Zigzag Pathway for Hot Carrier Collection with Graphene Electrode. *J. Phys. Chem. Lett.* **2021**, *12* (11), 2886–2891. https://doi.org/10.1021/acs.jpclett.1c00347.
(42) Chen, S.; Shi, G. Two-Dimensional Materials for Halide Perovskite-Based Optoelectronic Devices. *Adv. Mater.* **2017**, *29* (24), 1605448. https://doi.org/10.1002/adma.201605448.

(43) Shrestha, S.; Fischer, R.; Matt, G. J.; Feldner, P.; Michel, T.; Osvet, A.; Levchuk, I.; Merle, B.; Golkar, S.; Chen, H.; Tedde, S. F.; Schmidt, O.; Hock, R.; Rührig, M.; Göken, M.; Heiss, W.; Anton, G.; Brabec, C. J. High-Performance Direct Conversion X-Ray Detectors Based on Sintered Hybrid Lead Triiodide Perovskite Wafers. *Nature Photon* **2017**, *11* (7), 436–440. https://doi.org/10.1038/nphoton.2017.94.

(44) Hu, M.; Jia, S.; Liu, Y.; Cui, J.; Zhang, Y.; Su, H.; Cao, S.; Mo, L.; Chu, D.; Zhao, G.; Zhao, K.; Yang, Z.; Liu, S. F. Large and Dense Organic–Inorganic Hybrid Perovskite $CH_3NH_3PbI_3$ Wafer Fabricated by One-Step Reactive Direct Wafer Production with High X-Ray Sensitivity. *ACS Appl. Mater. Interfaces* **2020**, *12* (14), 16592–16600. https://doi.org/10.1021/acsami.9b23158.

(45) Deumel, S.; van Breemen, A.; Gelinck, G.; Peeters, B.; Maas, J.; Verbeek, R.; Shanmugam, S.; Akkerman, H.; Meulenkamp, E.; Huerdler, J. E.; Acharya, M.; García-Batlle, M.; Almora, O.; Guerrero, A.; Garcia-Belmonte, G.; Heiss, W.; Schmidt, O.; Tedde, S. F. High-Sensitivity High-Resolution X-Ray Imaging with Soft-Sintered Metal Halide Perovskites. *Nat Electron* **2021**, *4* (9), 681–688. https://doi.org/10.1038/s41928-021-00644-3.

(46) Spina, M.; Lehmann, M.; Náfrádi, B.; Bernard, L.; Bonvin, E.; Gaál, R.; Magrez, A.; Forró, L.; Horváth, E. Microengineered $CH_3NH_3PbI_3$ Nanowire/Graphene Phototransistor for Low-Intensity Light Detection at Room Temperature. *Small* **2015**, *11* (37), 4824–4828. https://doi.org/10.1002/smll.201501257.

(47) Šepelák, V.; Bégin-Colin, S.; Le Caër, G. Transformations in Oxides Induced by High-Energy Ball-Milling. *Dalton Trans.* **2012**, *41* (39), 11927. https://doi.org/10.1039/c2dt30349c.

(48) Saparov, B.; Mitzi, D. B. Organic–Inorganic Perovskites: Structural Versatility for Functional Materials Design. *Chem. Rev.* **2016**, *116* (7), 4558–4596. https://doi.org/10.1021/acs.chemrev.5b00715.

(49) Chen, J.; Zhou, S.; Jin, S.; Li, H.; Zhai, T. Crystal Organometal Halide Perovskites with Promising Optoelectronic Applications. *J. Mater. Chem. C* **2016**, *4* (1), 11–27. https://doi.org/10.1039/C5TC03417E.

(50) Posudievsky, O. Yu.; Konoshchuk, N. V.; Shkavro, A. G.; Karbivskiy, V. L.; Koshechko, V. G.; Pokhodenko, V. D. Nanostructured Mechanochemically Prepared Hybrid Perovskites Based on PbI_2 and Alkylammonium Halides for Optoelectronic Applications. *ACS Appl. Nano Mater.* **2018**, *1* (8), 4145–4155. https://doi.org/10.1021/acsanm.8b00881.

(51) Li, J.; Wang, H.; Chin, X. Y.; Dewi, H. A.; Vergeer, K.; Goh, T. W.; Lim, J. W. M.; Lew, J. H.; Loh, K. P.; Soci, C.; Sum, T. C.; Bolink, H. J.; Mathews, N.; Mhaisalkar, S.; Bruno, A. Highly Efficient Thermally Co-Evaporated Perovskite Solar Cells and Mini-Modules. *Joule* **2020**, *4* (5), 1035–1053. https://doi.org/10.1016/j.joule.2020.03.005.

(52) Halder, A.; Chulliyil, R.; Subbiah, A. S.; Khan, T.; Chattoraj, S.; Chowdhury, A.; Sarkar, S. K. Pseudohalide (SCN^-)-Doped $MAPbI_3$ Perovskites: A Few Surprises. *J. Phys. Chem. Lett.* **2015**, *6* (17), 3483–3489. https://doi.org/10.1021/acs.jpclett.5b01327.

(53) Atourki, L.; Vega, E.; Marí, B.; Mollar, M.; Ait Ahsaine, H.; Bouabid, K.; Ihlal, A. Role of the Chemical Substitution on the Structural and Luminescence Properties of the Mixed Halide Perovskite Thin MAPbI3−xBrx ($0 \leq x \leq 1$) Films. *Applied Surface Science* **2016**, *371*, 112–117. https://doi.org/10.1016/j.apsusc.2016.02.207.

(54) Ghimire, S.; Takahashi, K.; Takano, Y.; Nakamura, T.; Biju, V. Photon Recycling by Energy Transfer in Piezochemically Synthesized and Close-Packed Methylammonium Lead Halide Perovskites. *J. Phys. Chem. C* **2019**, *123* (45), 27752–27758. https://doi.org/10.1021/acs.jpcc.9b07003.

(55) Bonomi, S.; Tredici, I.; Albini, B.; Galinetto, P.; Rizzo, A.; Listorti, A.; Tamburini, U. A.; Malavasi, L. Ambient Condition Retention of Band-Gap Tuning in MAPbI $_3$ Induced by High Pressure Quenching. *Chem. Commun.* **2018**, *54* (94), 13212–13215. https://doi.org/10.1039/C8CC08549H.
(56) Yamada, T.; Yamada, Y.; Kanemitsu, Y. Photon Recycling in Perovskite CH3NH3PbX3 (X = I, Br, Cl) Bulk Single Crystals and Polycrystalline Films. *Journal of Luminescence* **2020**, *220*, 116987. https://doi.org/10.1016/j.jlumin.2019.116987.
(57) Li, Y.; Yan, W.; Li, Y.; Wang, S.; Wang, W.; Bian, Z.; Xiao, L.; Gong, Q. Direct Observation of Long Electron-Hole Diffusion Distance in CH3NH3PbI3 Perovskite Thin Film. *Sci Rep* **2015**, *5* (1), 14485. https://doi.org/10.1038/srep14485.
(58) D'Innocenzo, V.; Srimath Kandada, A. R.; De Bastiani, M.; Gandini, M.; Petrozza, A. Tuning the Light Emission Properties by Band Gap Engineering in Hybrid Lead Halide Perovskite. *J. Am. Chem. Soc.* **2014**, *136* (51), 17730–17733. https://doi.org/10.1021/ja511198f.
(59) Herz, L. M. Charge-Carrier Mobilities in Metal Halide Perovskites: Fundamental Mechanisms and Limits. *ACS Energy Lett.* **2017**, *2* (7), 1539–1548. https://doi.org/10.1021/acsenergylett.7b00276.
(60) Crothers, T. W.; Milot, R. L.; Patel, J. B.; Parrott, E. S.; Schlipf, J.; Müller-Buschbaum, P.; Johnston, M. B.; Herz, L. M. Photon Reabsorption Masks Intrinsic Bimolecular Charge-Carrier Recombination in CH $_3$ NH $_3$ PbI $_3$ Perovskite. *Nano Lett.* **2017**, *17* (9), 5782–5789. https://doi.org/10.1021/acs.nanolett.7b02834.
(61) de Quilettes, D. W.; Vorpahl, S. M.; Stranks, S. D.; Nagaoka, H.; Eperon, G. E.; Ziffer, M. E.; Snaith, H. J.; Ginger, D. S. Impact of Microstructure on Local Carrier Lifetime in Perovskite Solar Cells. *Science* **2015**, *348* (6235), 683–686. https://doi.org/10.1126/science.aaa5333.
(62) Wright, A. D.; Milot, R. L.; Eperon, G. E.; Snaith, H. J.; Johnston, M. B.; Herz, L. M. Band-Tail Recombination in Hybrid Lead Iodide Perovskite. *Adv. Funct. Mater.* **2017**, *27* (29), 1700860. https://doi.org/10.1002/adfm.201700860.
(63) Witt, C.; Leupold, N.; Ramming, P.; Schötz, K.; Moos, R.; Panzer, F. How the Microstructure of MAPbI $_3$ Powder Impacts Pressure-Induced Compaction and Optoelectronic Thick-Film Properties. *J. Phys. Chem. C* **2022**, *126* (36), 15424–15435. https://doi.org/10.1021/acs.jpcc.2c03329.
(64) Stranks, S. D.; Snaith, H. J. Metal-Halide Perovskites for Photovoltaic and Light-Emitting Devices. *Nature Nanotech* **2015**, *10* (5), 391–402. https://doi.org/10.1038/nnano.2015.90.
(65) Schötz, K.; Askar, A. M.; Köhler, A.; Shankar, K.; Panzer, F. Investigating the Tetragonal-to-Orthorhombic Phase Transition of Methylammonium Lead Iodide Single Crystals by Detailed Photoluminescence Analysis. *Adv. Optical Mater.* **2020**, *8* (17), 2000455. https://doi.org/10.1002/adom.202000455.
(66) Kim, S.-Y.; Lee, H.-C.; Nam, Y.; Yun, Y.; Lee, S.-H.; Kim, D. H.; Noh, J. H.; Lee, J.-H.; Kim, D.-H.; Lee, S.; Heo, Y.-W. Ternary Diagrams of the Phase, Optical Bandgap Energy and Photoluminescence of Mixed-Halide Perovskites. *Acta Materialia* **2019**, *181*, 460–469. https://doi.org/10.1016/j.actamat.2019.10.008.
(67) Minussi, F. B.; A. Silva, L.; Araújo, E. B. Structure, Optoelectronic Properties and Thermal Stability of the Triple Organic Cation GA $_x$ FA $_x$ MA $_{1-2x}$ PbI $_3$ System Prepared by Mechanochemical Synthesis. *Phys. Chem. Chem. Phys.* **2022**, *24* (8), 4715–4728. https://doi.org/10.1039/D1CP04977A.
(68) Diab, H.; Arnold, C.; Lédée, F.; Trippé-Allard, G.; Delport, G.; Vilar, C.; Bretenaker, F.; Barjon, J.; Lauret, J.-S.; Deleporte, E.; Garrot, D. Impact of Reabsorption on the Emission

Spectra and Recombination Dynamics of Hybrid Perovskite Single Crystals. *J. Phys. Chem. Lett.* **2017**, *8* (13), 2977–2983. https://doi.org/10.1021/acs.jpclett.7b00998.
(69) Gerber, O.; Pichon, B. P.; Ulhaq, C.; Grenèche, J.-M.; Lefevre, C.; Florea, I.; Ersen, O.; Begin, D.; Lemonnier, S.; Barraud, E.; Begin-Colin, S. Low Oxidation State and Enhanced Magnetic Properties Induced by Raspberry Shaped Nanostructures of Iron Oxide. *The Journal of Physical Chemistry C* **2015**, *119* (43), 24665–24673. https://doi.org/10.1021/acs.jpcc.5b08164.
(70) Gerber, O.; Pichon, B. P.; Ihiawakrim, D.; Florea, I.; Moldovan, S.; Ersen, O.; Begin, D.; Grenèche, J.-M.; Lemonnier, S.; Barraud, E.; Begin-Colin, S. Synthesis Engineering of Iron Oxide Raspberry-Shaped Nanostructures. *Nanoscale* **2017**, *9* (1), 305–313. https://doi.org/10.1039/C6NR07567C.
(71) Chen, S.; Gao, P. Challenges, Myths, and Opportunities of Electron Microscopy on Halide Perovskites. *Journal of Applied Physics* **2020**, *128* (1), 010901. https://doi.org/10.1063/5.0012310.
(72) Baikie, T.; Fang, Y.; Kadro, J. M.; Schreyer, M.; Wei, F.; Mhaisalkar, S. G.; Graetzel, M.; White, T. J. Synthesis and Crystal Chemistry of the Hybrid Perovskite (CH3NH3)PbI3 for Solid-State Sensitised Solar Cell Applications. *J. Mater. Chem. A* **2013**, *1* (18), 5628. https://doi.org/10.1039/c3ta10518k.
(73) Eckmann, A.; Felten, A.; Mishchenko, A.; Britnell, L.; Krupke, R.; Novoselov, K. S.; Casiraghi, C. Probing the Nature of Defects in Graphene by Raman Spectroscopy. *Nano Lett.* **2012**, *12* (8), 3925–3930. https://doi.org/10.1021/nl300901a.
(74) Chacón-Torres, J. C.; Wirtz, L.; Pichler, T. Manifestation of Charged and Strained Graphene Layers in the Raman Response of Graphite Intercalation Compounds. *ACS Nano* **2013**, *7* (10), 9249–9259. https://doi.org/10.1021/nn403885k.
(75) Niemann, R. G.; Kontos, A. G.; Palles, D.; Kamitsos, E. I.; Kaltzoglou, A.; Brivio, F.; Falaras, P.; Cameron, P. J. Halogen Effects on Ordering and Bonding of $CH_3NH_3^+$ in $CH_3NH_3PbX_3$ (X = Cl, Br, I) Hybrid Perovskites: A Vibrational Spectroscopic Study. *J. Phys. Chem. C* **2016**, *120* (5), 2509–2519. https://doi.org/10.1021/acs.jpcc.5b11256.
(76) Castaneda, J. F.; Im, J.-H.; Liu, Y.; Liu, S.; Park, N.-G.; Zhang, Y. Domain Size, Temperature, and Time Dependence of Photodegradation in $MAPbI_3$ Probed by Raman Spectroscopy. *ACS Energy Lett.* **2022**, *7* (9), 3095–3103. https://doi.org/10.1021/acsenergylett.2c01640.
(77) Chen, Q.; Liu, H.; Kim, H.-S.; Liu, Y.; Yang, M.; Yue, N.; Ren, G.; Zhu, K.; Liu, S.; Park, N.-G.; Zhang, Y. Multiple-Stage Structure Transformation of Organic-Inorganic Hybrid Perovskite CH 3 NH 3 PbI 3. *Phys. Rev. X* **2016**, *6* (3), 031042. https://doi.org/10.1103/PhysRevX.6.031042.
(78) Pistor, P.; Ruiz, A.; Cabot, A.; Izquierdo-Roca, V. Advanced Raman Spectroscopy of Methylammonium Lead Iodide: Development of a Non-Destructive Characterisation Methodology. *Sci Rep* **2016**, *6* (1), 35973. https://doi.org/10.1038/srep35973.
(79) Quarti, C.; Grancini, G.; Mosconi, E.; Bruno, P.; Ball, J. M.; Lee, M. M.; Snaith, H. J.; Petrozza, A.; De Angelis, F. The Raman Spectrum of the $CH_3NH_3PbI_3$ Hybrid Perovskite: Interplay of Theory and Experiment. *J. Phys. Chem. Lett.* **2014**, *5* (2), 279–284. https://doi.org/10.1021/jz402589q.
(80) Ling, X.; Xie, L.; Fang, Y.; Xu, H.; Zhang, H.; Kong, J.; Dresselhaus, M. S.; Zhang, J.; Liu, Z. Can Graphene Be Used as a Substrate for Raman Enhancement? *Nano Lett.* **2010**, *10* (2), 553–561. https://doi.org/10.1021/nl903414x.
(81) Kim, J.-H.; Van Le, Q.; Nguyen, T. P.; Lee, T. H.; Jang, H. W.; Yun, W. S.; Jeong, S. M.; Lee, J.; Kim, S. Y.; Kim, H. Graphene-Mediated Enhanced Raman Scattering and

Coherent Light Lasing from CsPbI3 Perovskite Nanorods. *Nano Energy* **2020**, *70*, 104497. https://doi.org/10.1016/j.nanoen.2020.104497.
(82) Ling, X.; Moura, L. G.; Pimenta, M. A.; Zhang, J. Charge-Transfer Mechanism in Graphene-Enhanced Raman Scattering. *J. Phys. Chem. C* **2012**, *116* (47), 25112–25118. https://doi.org/10.1021/jp3088447.
(83) Liu, Y.; Yang, Z.; Cui, D.; Ren, X.; Sun, J.; Liu, X.; Zhang, J.; Wei, Q.; Fan, H.; Yu, F.; Zhang, X.; Zhao, C.; Liu, S. F. Two-Inch-Sized Perovskite $CH_3NH_3PbX_3$ (X = Cl, Br, I) Crystals: Growth and Characterization. *Adv. Mater.* **2015**, *27* (35), 5176–5183. https://doi.org/10.1002/adma.201502597.
(84) Stranks, S. D.; Eperon, G. E.; Grancini, G.; Menelaou, C.; Alcocer, M. J. P.; Leijtens, T.; Herz, L. M.; Petrozza, A.; Snaith, H. J. Electron-Hole Diffusion Lengths Exceeding 1 Micrometer in an Organometal Trihalide Perovskite Absorber. *Science* **2013**, *342* (6156), 341–344. https://doi.org/10.1126/science.1243982.
(85) Xing, G.; Mathews, N.; Sun, S.; Lim, S. S.; Lam, Y. M.; Grätzel, M.; Mhaisalkar, S.; Sum, T. C. Long-Range Balanced Electron- and Hole-Transport Lengths in Organic-Inorganic $CH_3NH_3PbI_3$. *Science* **2013**, *342* (6156), 344–347. https://doi.org/10.1126/science.1243167.
(86) Villamil Franco, C. Ultrafast Dynamics of Excitons and Charge Carriers in Colloidal Perovskite Nanostructures Studied by Time-Resolved Optical Spectroscopies, Université Paris-Saclay, CEA, CNRS, LIDYL, 2020. https://theses.hal.science/tel-03222108.
(87) Johnston, M. B.; Herz, L. M. Hybrid Perovskites for Photovoltaics: Charge-Carrier Recombination, Diffusion, and Radiative Efficiencies. *Acc. Chem. Res.* **2016**, *49* (1), 146–154. https://doi.org/10.1021/acs.accounts.5b00411.
(88) Delport, G.; Chehade, G.; Lédée, F.; Diab, H.; Milesi-Brault, C.; Trippé-Allard, G.; Even, J.; Lauret, J.-S.; Deleporte, E.; Garrot, D. Exciton–Exciton Annihilation in Two-Dimensional Halide Perovskites at Room Temperature. *J. Phys. Chem. Lett.* **2019**, *10* (17), 5153–5159. https://doi.org/10.1021/acs.jpclett.9b01595.
(89) Pelant, I.; Valenta, J. *Luminescence Spectroscopy of Semiconductors*, 1st ed.; Oxford University PressOxford, 2012. https://doi.org/10.1093/acprof:oso/9780199588336.001.0001.
(90) He, M.; Chen, Y.; Liu, H.; Wang, J.; Fang, X.; Liang, Z. Chemical Decoration of $CH_3NH_3PbI_3$ Perovskites with Graphene Oxides for Photodetector Applications. *Chem. Commun.* **2015**, *51* (47), 9659–9661. https://doi.org/10.1039/C5CC02282G.
(91) Pisoni, A.; Jaćimović, J.; Barišić, O. S.; Spina, M.; Gaál, R.; Forró, L.; Horváth, E. Ultra-Low Thermal Conductivity in Organic–Inorganic Hybrid Perovskite $CH_3NH_3PbI_3$. *J. Phys. Chem. Lett.* **2014**, *5* (14), 2488–2492. https://doi.org/10.1021/jz5012109.
(92) Baussens, O.; Maturana, L.; Amari, S.; Zaccaro, J.; Verilhac, J.-M.; Hirsch, L.; Gros-Daillon, E. An Insight into the Charge Carriers Transport Properties and Electric Field Distribution of $CH_3NH_3PbBr_3$ Thick Single Crystals. *Appl. Phys. Lett.* **2020**, *117* (4), 041904. https://doi.org/10.1063/5.0011713.
(93) García-Batlle, M.; Deumel, S.; Huerdler, J. E.; Tedde, S. F.; Guerrero, A.; Almora, O.; Garcia-Belmonte, G. Mobile Ion-Driven Modulation of Electronic Conductivity Explains Long-Timescale Electrical Response in Lead Iodide Perovskite Thick Pellets. *ACS Appl. Mater. Interfaces* **2021**, *13* (30), 35617–35624. https://doi.org/10.1021/acsami.1c06046.
(94) Wang, L.; Yuan, G. D.; Duan, R. F.; Huang, F.; Wei, T. B.; Liu, Z. Q.; Wang, J. X.; Li, J. M. Tunable Bandgap in Hybrid Perovskite CH3NH3Pb(Br3−yXy) Single Crystals and Photodetector Applications. *AIP Advances* **2016**, *6* (4), 045115. https://doi.org/10.1063/1.4948312.

(95) Murali, B.; Saidaminov, M. I.; Abdelhady, A. L.; Peng, W.; Liu, J.; Pan, J.; Bakr, O. M.; Mohammed, O. F. Robust and Air-Stable Sandwiched Organo-Lead Halide Perovskites for Photodetector Applications. *J. Mater. Chem. C* **2016**, *4* (13), 2545–2552. https://doi.org/10.1039/C6TC00610H.
(96) Sun, M.; Fang, Q.; Zhang, Z.; Xie, D.; Sun, Y.; Xu, J.; Li, W.; Ren, T.; Zhang, Y. All-Inorganic Perovskite Nanowires–InGaZnO Heterojunction for High-Performance Ultraviolet–Visible Photodetectors. *ACS Appl. Mater. Interfaces* **2018**, *10* (8), 7231–7238. https://doi.org/10.1021/acsami.7b17935.
(97) Deng, H.; Yang, X.; Dong, D.; Li, B.; Yang, D.; Yuan, S.; Qiao, K.; Cheng, Y.-B.; Tang, J.; Song, H. Flexible and Semitransparent Organolead Triiodide Perovskite Network Photodetector Arrays with High Stability. *Nano Lett.* **2015**, *15* (12), 7963–7969. https://doi.org/10.1021/acs.nanolett.5b03061.
(98) Ciavatti, A.; Sorrentino, R.; Basiricò, L.; Passarella, B.; Caironi, M.; Petrozza, A.; Fraboni, B. High-Sensitivity Flexible X-Ray Detectors Based on Printed Perovskite Inks. *Adv Funct Materials* **2021**, *31* (11), 2009072. https://doi.org/10.1002/adfm.202009072.
(99) Liu, C.-H.; Chang, Y.-C.; Norris, T. B.; Zhong, Z. Graphene Photodetectors with Ultra-Broadband and High Responsivity at Room Temperature. *Nature Nanotech* **2014**, *9* (4), 273–278. https://doi.org/10.1038/nnano.2014.31.

For Table of contents only